ATOMISTIC SIMULATIONS OF THE MECHANICAL DEFORMATION AND ENERGETICS OF METAL NANOWIRES

A Dissertation
Presented to
The Academic Faculty

by

Austin M. Leach

In Partial Fulfillment
of the Requirements for the Degree
Doctor of Philosophy in the
School of Materials Science and Engineering

Georgia Institute of Technology
December 2007

ATOMISTIC SIMULATIONS OF THE MECHANICAL DEFORMATION AND ENERGETICS OF METAL NANOWIRES

Approved by:

Dr. Ken Gall, Advisor
Materials Science and Engineering
Georgia Institute of Technology

Dr. Tom Sanders
Materials Science and Engineering
Georgia Institute of Technology

Dr. Mo Li
Materials Science and Engineering
Georgia Institute of Technology

Dr. Ting Zhu
Mechanical Engineering
Georgia Institute of Technology

Dr. Elisa Riedo
Physics
Georgia Institute of Technology

Date Approved: August 21, 2007

To my family, friends, and the advancement of science.

TABLE OF CONTENTS

Page

LIST OF TABLES *vii*

LIST OF FIGURES *ix*

LIST OF SYMBOLS AND ABBREVIATIONS *xi*

SUMMARY *xiv*

CHAPTER

I INTRODUCTION 1

1.1 Motivation 1

1.2 Research Objectives 4

1.3 Dissertation Structure 5

II ATOMISTIC SIMULATION METHODOLOGY 7

2.1 Introduction 7

2.2 Molecular statics calculations 9

2.3 Molecular dynamics calculations 10

2.4 Embedded-atom method potential 12

2.5 Simulation boundary conditions 14

2.6 Application of atomistic simulations 15

2.6.1 Atomistic simulation precursors 15

2.6.2 Energetics of mechanical deformation 16

2.6.3 General loading procedures 18

2.6.3.1 Molecular statics loading procedure 18

2.6.3.2 Molecular dynamics loading procedure 19

2.7 Stacking fault energy in atomistic simulations 20

2.7.1 Calculation of generalized stacking fault curves 21

III TENSILE DEFORMATION OF TOP-DOWN AND BOTTOM-UP NANOWIRES 25

3.1 Introduction 25

3.2 Simulation methodology 30

3.3 Results 34

3.3.1 Top-down rhombic silver nanowires 36

3.3.2 Top-down truncated-rhombic silver nanowires 39

3.3.3 Bottom-up pentagonal silver nanowires 41

3.3.4 Size effect on yield strength 46

3.4 Discussion 47

3.4.1 Top-down deformation behavior 47

3.4.2 Bottom-up deformation behavior 50

3.4.3 Size effect on yield strength 51

3.5 Conclusion 53

IV ELASTIC BENDING BEHAVIOR OF METAL NANOWIRES 55

4.1 Introduction 55

4.2 Methodology 58

4.2.1 Computational techniques 60

4.2.2 Calculation of the elastic modulus 62

4.3 Results and discussion 66

4.4 Summary and conclusions 73

V ENERGY LANDSCAPES OF DEFORMATION PATHWAYS IN METAL NANOWIRES 75

5.1 Introduction 75

5.2 Simulation methodology 78

5.2.1 Nanowire geometries 79
5.2.2 Molecular dynamics procedures 79
5.2.3 Molecular statics procedures 81
5.2.4 Deformation pathways 82
5.3 Results 83
5.3.1 Operant deformation mechanisms 83
5.3.2 Energy landscapes of twinning and slip 87
5.4 Discussion 88
5.5 Conclusions 90
REFERENCES 91

LIST OF TABLES

Page

Table 2.1: Fitting parameters for the Voter and Chen EAM potential 14

Table 3.1: Geometric parameters and relative stability of simulated nanowires 34

Table 5.1: Surface energies for the low-index surfaces of silver 89

LIST OF FIGURES

Page

Figure 1.1: TEM image of a *top-down* gold nanowire 2

Figure 1.2: SEM image of an array of pentagonal silver nanowires 2

Figure 2.1: Schematic of the potential energy of a materials system 17

Figure 2.2: Atomic configurations obtained during the calculation of a GSF 23

Figure 2.3: GSF curve for the Voter-Chen silver EAM potential 24

Figure 3.1: Schematic of the mechanical response of bulk and nanometer scale monolithic metals under force and displacement control tensile loading 26

Figure 3.2: Geometries and crystallographic properties of *top-down* and *bottom-up* nanowires 33

Figure 3.3: Stress-strain response of *top-down* and *bottom-up* nanowires 35

Figure 3.4: Snapshots of a rhombic silver nanowire during tensile deformation 37

Figure 3.5: Stacking fault formation and twin propagation in a rhombic silver nanowire 38

Figure 3.6: Snapshots of a truncated-rhombic silver nanowire during tensile deformation 41

Figure 3.7: Stacking fault formation and partial dislocation propagation in a truncated-rhombic silver nanowire 43

Figure 3.8: Snapshots of a pentagonal silver nanowire during tensile deformation 44

Figure 3.9: Outer shell fracture and partial dislocation nucleation in a pentagonal silver nanowire 45

Figure 3.10: Size effect on the tensile yield strength of top-down and bottom-up silver nanowires 46

Figure 4.1: Geometries and crystallographic properties of nanowires subjected to bending deformation 59

Figure 4.2: Schematic showing the bending process 60

Figure 4.3: Theoretical and actual deflection profiles for a representative nanowire subjected to bending 63

Figure 4.4: Young's modulus values obtained from bending and tension of <110> and <100> nanowires 67

Figure 4.5: Percent difference in the modulus values for bending and tension 68

Figure 5.1: Schematic portraying the total energy of a material 76

Figure 5.2: Geometry and crystallographic structure of rhombic-type nanowires 80

Figure 5.3: Atomic configurations for a perfect rhombic nanowire undergoing deformation twinning 84

Figure 5.4: Atomic configurations for a truncated-rhombic nanowire undergoing slip 85

Figure 5.5: Structure and geometry of rhombic and truncated-rhombic nanowires before and after reorientation by deformation twinning 86

Figure 5.6: Energy landscapes for twinning and slip in rhombic-type nanowires 87

LIST OF SYMBOLS AND ABBREVIATIONS

AFM	Atomic force microscope
BCT	Body-centered tetragonal
EAM	Embedded-atom method
FCC	Face-centered cubic
GSF	Generalized stacking fault
HRTEM	High-resolution transmission electron microscope
MD	Molecular dynamics
MEAM	Modified embedded-atom method
MS	Molecular statics
SEM	Scanning electron microscope
TEM	Transmission electron microscope
a_o	Equilibrium lattice constant
B	Bulk modulus
C_{11}, C_{12}, C_{44}	Cubic elastic constants
D	Nanowire diameter
D_e	Diatomic molecule bond strength
ΔE_{vf}	Vacancy formation energy
ΔU	Strain energy
E	Elastic modulus
$E_{\{100\}}$	Energy of the {100} FCC surface
$E_{\{110\}}$	Energy of the {110} FCC surface

$E_{\{111\}}$	Energy of the {111} FCC surface
E_b	Elastic modulus from bending
E_{coh}	Cohesive energy
E_{core}	Energy of a nanowire core
$E_{surface}$	Total surface energy of a nanowire
E_t	Elastic modulus from tension
E_{total}	Total energy of a nanowire
F	Force acting on a nanowire under tension
F_i^{α}	Force acting on atom i in the α direction
h	Height of a nanowire cross-section
I	Moment of inertia
L	Length of a nanowire
m_i	Mass of atom i
N	Total number of atoms in a simulation
P	Bending load on a nanowire
R_e	Diatomic molecule bond length
R_{ij}	Distance between atom i and atom j
S	Cross-sectional area of a nanowire
T	Temperature
U	Total potential energy of a system of atoms
V	Volume of a system of atoms
V_0	Initial volume of a system of atoms
x, y, z	Cartesian coordinates

x_i^{α}	Cartesian coordinate of atom i in the α direction
δ_B	Maximum deflection of a nanowire under bending
ε	Tensile strain
ϕ_{ij}	Short range pair interaction between atoms i and j
γ_{esf}	Extrinsic stacking fault energy
γ_{isf}	Intrinsic stacking fault energy
γ_{usf}	Unstable stacking fault energy
γ_{ut}	Unstable twinning energy
ν	Deflection of a nanowire under bending
$\bar{\rho}_i$	Spherically averaged electron density
σ	Axial stress

SUMMARY

Nanowires are an exciting class of novel materials that have potential applications in areas including biological sensing, photonics, and electronics. The promise of these future applications relies on the production of nanowires of controlled size, shape, and crystal structure, in reasonable quantities, and further, ultimately requires that the nanowires be mechanically stable in the application environment. This research is aimed at understanding the mechanical behavior of metallic nanowires, through the use of atomistic simulations.

At the nanometer scale, where the surface-area-to-volume ratio is substantial, the effects of free surfaces have a primary influence on the physical properties of a material. Surface energy arises from unsatisfied bond coordination at the surface of a solid and results in a surface stress as the surface atoms contract into the bulk of the material to increase their local electron density. The magnitude of surface energy and surface stress is dependent on the orientation of the surface and the compliance of the structure. In bulk materials, the effects of surfaces are negligible; however, at the nanometer scale, surface effects become quite significant.

In metallic nanowires, these surface effects strongly influence mechanical properties, and the characteristics of plastic deformation. The mechanical testing of nanowires is precluded by the difficulties of accurately applying and measuring forces on the nanometer scale. For this reason, computational simulations are a primary tool for investigating the mechanical behavior of nanowires. In this work, we have performed

atomistic simulations to examine the mechanical response of silver nanowires. We have conducted studies to determine the deformation characteristics of experimentally observed nanowire geometries subjected to tensile and bending loads. We have also developed a technique to probe the energetics of mechanical deformation, in order to elucidate the energetically favored deformation pathways in nanowires. Our results show that nanowires may be tailored for specific mechanical requirements based on geometry and free surface orientation and provide insight to the effect of free surfaces in the mechanical deformation of nanometer scale structures.

CHAPTER I

INTRODUCTION

1.1 Motivation

Metallic nanostructures are of significant interest in materials engineering because of their potential application in small devices and because they exhibit 'special' properties relative to their bulk counterparts [1, 2]. In particular, one-dimensional nanostructures [3] have promising applications in electronics [4-6], photonics [7, 8], biologically inspired nanocomposites [9-11], chemical sensing and imaging [12, 13], and even drug delivery [14]. In addition to favorable functional properties, nanometer scale metallic wires show extraordinarily high combinations of strength, stiffness, and ductility relative to bulk materials.

All of the promise of these future applications rely on production of nanowires of controlled size, shape, and crystal structure, in reasonable quantities, and further, ultimately requires that the nanowires be *mechanically stable* in the application environment. Enormous progress has been made in the synthesis of nanowires [3], particularly in the case of nanowires fabricated from face-centered-cubic (FCC) metals. Metal nanowires have been fabricated using both *top-down* and *bottom-up* techniques. *Top-down* methods involve extraction of a nanowire from a bulk sample through processes such as electron beam lithography [15, 16] or mechanical area reduction, while *bottom-up* classifies nanowires that have been grown through chemical or molecular assembly or by template assisted electro-deposition. [17-25] A gold nanowire fabricated

using a *top-down* approach is presented in Figure 1.1. An array of pentagonal nanowires produced using *bottom-up* methods is shown in Figure 1.2.

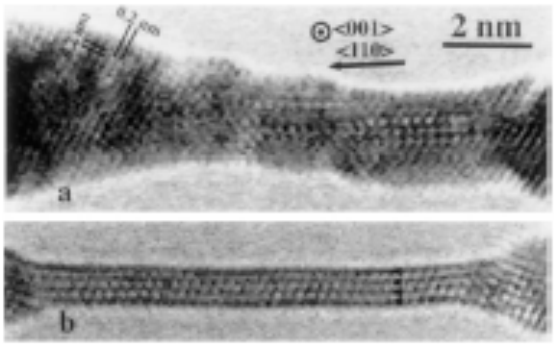

Figure 1.1: Transmission electron microscope (TEM) image of the formation of a gold nanowire. A gold film of 3 nm thickness and (001) orientation was bombarded with an electron beam to create closely spaced 'nanoholes' forming a stable 'nanobridge' (nanowire) in between The initial stage of formation is shown (top), and after further material removal, a ~1 nm nanowire is formed (bottom). Reproduced from [16].

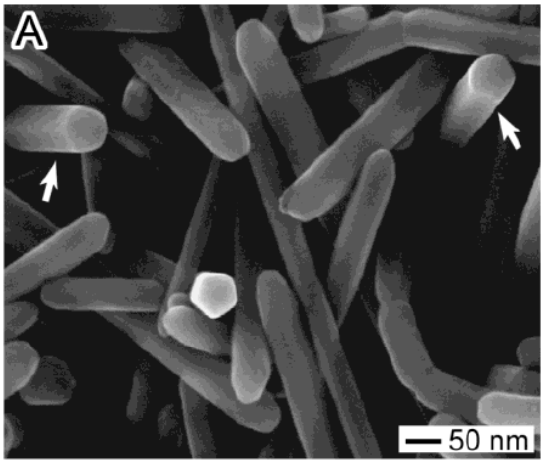

Figure 2.2: Scanning electron microscope (SEM) image of an array of pentagonal silver nanowires. The nanowires are approximately 30 nm in diameter, on average. Reproduced from [22].

The mechanical characterization of nanowires requires an understanding of material strength in the most basic form. Fundamentally, the strength of a material is determined by the arrangement of its constituents and the interactions between them. Thus, the resistance of a material to deformation is established by its atomic structure and the cohesion within. This concept of strength is irrespective of length scale, yet nanometer scale materials exhibit a drastically different mechanical response than their bulk counterparts [10, 11, 26, 27]. This is primarily due to the influence of free surfaces.

At the nanometer scale, where the surface-area-to-volume ratio is substantial, the effects of free surfaces have a primary influence on the physical properties of a material. These 'surface effects' are ubiquitous in the deformation of nanowires. Surface energy arises from unsatisfied bond coordination at the surface of a solid and results in a surface stress as the surface atoms contract into the bulk of the material to increase their local electron density. Surface stress is obtained as the strain derivative of surface energy, and varies in magnitude, depending on the orientation of the surface, and the compliance of the structure. In bulk materials, the effects of surface stress are negligible; however, at the nanometer scale, surface stresses become quite significant.

The mechanical properties of metallic nanowires are not well established due to the complexities of mechanical testing presented at the nanometer size regime. Currently, atomistic simulations are the primary tool for investigating the mechanical deformation of nanowires and the associated mechanisms. Specifically, the embedded-atom method (EAM) [28] has been extensively applied to investigate the mechanical response of nanowires [29-37]. Many of these atomistic simulations have focused on characterizing the influence of free surfaces on the stability and mechanical properties of

metal nanowires. It has been shown that surface stresses from exposed high-energy (100) surfaces in gold nanowires can lead to mechanical instability as the cross-section is reduced [29, 30]. In these studies, gold nanowires were predicted to undergo a phase transformation [29] from FCC to body-centered tetragonal (BCT) or a lattice reorientation [30] from <100> to <110> along the axial direction, solely from the magnitude of the surface stress in the nanowire. Other studies have investigated the impact of free surfaces and nanowire geometry on the operant deformation mechanisms.[38, 39] The vast majority of these simulations have analyzed the mechanical response of nanowires subjected to uniaxial tensile and compressive loading. These simulations have indicated that the deformation behavior of metal nanowires is sensitive to the size of the nanowire and also to the crystallographic orientation of the free surfaces; however, they have provided only a qualitative understanding of this behavior. Also, previous computational studies have only considered hypothetical nanowire geometries and have lacked a direct connection with nanowire geometries synthesized using common *top-down* and *bottom-up* approaches.

1.2 Research Objectives

This research aims to answer the following questions relating to the mechanical behavior and energetics of metal nanowires:

1) Can we create atomistic models that accurately represent experimentally observed and fabricated nanowire geometries?
2) What is the mechanical response of realistic nanowire geometries under tensile loads?

3) What is the mechanical response of realistic nanowire geometries under bending loads?

4) Can we quantify the effect of free surfaces on operant deformation mechanisms in metal nanowires?

1.3 Dissertation Structure

This dissertation is arranged into individual chapters that address the research objectives presented in section 1.2. Each chapter (with the exception of Chapter 1) is summarized below.

Chapter 2 presents the methodology of atomistic simulations. The fundamental theories behind MS and MD are covered, as well as the specific formulation of the EAM. Also included in this chapter are simulation specific methodologies, which include the general mechanical loading procedures for each type of simulation.

In Chapter 3 the tensile deformation of *top-down* and *bottom-up* silver nanowires is presented. We considered the deformation of three different nanowire geometries, from an initial, defect-free configuration to failure. The overall deformation behavior is presented, and the mechanism responsible for incipient plasticity in each nanowire is analyzed in detail. This study revealed that the mechanical behavior of nanowires is strongly dependent on nanowire geometry. We also determined a geometry dependent size effect on the tensile yield strength in the nanowires. The major conclusion from this study is that the mechanical response of nanowires can be tailored for application in future devices based on nanowire size and geometry.

The elastic bending behavior of silver nanowires is discussed in Chapter 4. We considered two different axial orientations of nanowires and two different surface

orientations for each axial orientation in this analysis. Nanowires were modeled as cantilever beams, and the bending deformation was simulated within the elastic deformation regime. The elastic modulus of the nanowires was extracted from the calculated mechanical response using formulations from the fundamentals of continuum beam theory. The bending deformation was simulated for a range of nanowire sizes for each orientation, and the size effect on the bending modulus was determined. The results reveal that the bending modulus exhibits the same size dependence as the tensile modulus for nanowires larger than around 5 nm in diameter, and thus, that free surfaces are not preferentially sampled by bending deformation in nanowire sizes that fall within the current experimental testing capabilities.

Lastly, the surface effect on operant deformation mechanisms is analyzed using MS calculations. A technique is developed to 'map' the energetic pathways of various deformation mechanisms in *top-down* silver nanowire geometries. The study considers rhombic-type silver nanowires subjected to tensile deformation. The deformation was simulated in MD in order to deduce the energetically favored deformation pathway. Next, the two possible deformation pathways (twinning or slip) were simulated using MS calculations to determine the energetic landscape during the deformation process. This study reveals that the free surface orientation dictates whether a metal nanowire will undergo deformation twinning or partial-dislocation mediated 'slip'.

CHAPTER II

ATOMISTIC SIMULATION METHODOLOGY

2.1 Introduction

The role of computational modeling in materials science is ever increasing. In materials science, computer simulations allow the researcher to perform experiments under finely tuned conditions in order to determine the specific response of a material system to external stimuli. In the present study, we have employed atomistic simulations in order to elucidate the response of metallic nanowires to mechanical deformation. Two general types of atomistic simulations have been utilized in this work: molecular statics (MS) and molecular dynamics (MD). In this chapter, the underlying principles of these two classes of simulations will be explained, with a particular emphasis on the ability of these methods to accurately model the mechanics and energetics of metallic nanowires.

Atomistic simulations rely on the computation of the total energy of a material system, from which physical properties and quantities are extracted. There exist many different methods for calculating the total energy of a system of atoms, which range in complexity and computational expense. In computational materials science, the precision of the calculated parameters is indirectly proportional to computational demand. For instance, for any arrangement of atoms, the total energy of the system may be calculated by solving the time-independent Schrödinger equation. This solution would provide the highest attainable precision; however, even for systems with few atoms and the most advanced computational resources this is not realistic. A less computationally intensive

set of calculations involves an implicit consideration of the electronic structure of atoms, by utilizing various approximations to the Schrödinger equation. These *ab initio* techniques provide extremely precise calculations, but are limited to atomic systems such as clusters and other small nanometer scale structures containing fewer than around one-hundred atoms. In order to compute the total energy of larger systems, and of structures such as metallic nanowires, even further approximations must be introduced, where the electronic structure of atoms is only considered explicitly, through interatomic potentials.

The Born-Oppenheimer approximation to the time-independent Schrödinger equation provides the theoretical basis for the interatomic potential. The foundation of the Born-Oppenheimer approximation lies in the separation of the motions of electrons and nuclei. This is allowable, since the mass of the nucleus is much greater than that of the electron, and thus the timescale of nuclear motion is around two-orders of magnitude slower than that of electron motion.[40] In essence, this approximation allows the computation of the total energy of a system, based solely on the nuclear coordinates, thereby removing the electronic degrees of freedom in the system. The interatomic potential results, as it captures the parametric dependence of the potential energy on the nuclear coordinates of the system. The Born-Oppenheimer approximation introduces minimal error into atomistic calculations. For the diatomic hydrogen molecule, the error is on the order of 10^{-4}, and the error decreases as the size of the nucleus increases.[40] Thus, for metals, atomistic calculations using interatomic potentials have a solid foundation in the principles of quantum mechanics and may be performed within acceptable error, under this approximation.

Typically, in large-scale computational materials science, all electronic degrees of freedom are omitted from numerical calculations, and the system energy is calculated from the response of the atomic nuclei to small perturbations, as specified by the interatomic potential. Much effort has been undertaken to develop functional forms for the interatomic potential that accurately and realistically capture material behavior. This work utilizes the EAM type of interatomic potentials.

2.2 Molecular statics calculations

MS implies calculations that are performed in the absence of thermal contributions to the total energy of the system. When thermal vibrations are not considered, the system energy may be calculated independent of time, based solely on the positions of the atomic nuclei, according to the interatomic potential. In MS simulations, iterative optimization schemes are employed to determine the atomic positions that minimize the total potential energy of the system. A criterion is specified within the simulation framework to determine when the system energy has 'converged' upon the minimum energy value.

Many numerical optimization techniques have been used to perform MS calculations. These include the Monte Carlo method, genetic algorithms, and the conjugate gradient method. The MS simulations in this work were performed using conjugate gradient energy minimization. In conjunction with the interatomic potential, conjugate gradient energy minimization is performed according to the following steps:

1) for a given a set of atomic coordinates, the total energy of the system is calculated according to the interatomic potential

2) the atomic coordinates7 are rearranged, conjugate to the previous atomic positions

3) the total energy of the system is recalculated from the 'new' atomic positions

These steps outline the iterative procedure of energy minimization. For each atomic rearrangement, the atoms are moved conjugate to their former position, according to the direction of steepest decent on the potential energy curve of the system. This procedure is repeated until a minimum energy value is obtained, as dictated by the specified convergence criterion.

2.3 Molecular dynamics calculations

In MD simulations, a classical Newtonian trajectory is integrated over a period of time for a system of atoms, as dictated by the interatomic potential. In MD, for a system of N atoms with constant volume and constant total potential energy, the force on an atom may be computed by calculating the derivative of the total energy with respect to the position of the atom, and is given as:

$$F_i^{\alpha} = -\frac{\partial U}{\partial x_i^{\alpha}} \qquad i = 1,2,...,N \quad \alpha = 1,2,3 \tag{2.1}$$

where, U is the potential energy of the system, x_i^{α} is the Cartesian coordinate of atom i in the α direction, and F_i^{α} is the force acting on atom i in the α direction. The motion of the atoms is then calculated according to Newton's second law of motion:

$$m_i \frac{d^2 x_i^{\alpha}}{dt^2} = F_i^{\alpha} \qquad i = 1,2,...,N \quad \alpha = 1,2,3 \tag{2.2}$$

where m_i is the mass of atom i and t represents time. In atomistic simulations, the motion of atoms are not independent of one another, thus the equations of motion must be coupled. Since the equations of motion are coupled, they must be solved using numerical methods. The MD simulations in this work utilize the Verlet finite difference method to perform this task. The derivation of the Verlet method involves a forward and reverse Taylor series expansion of the atomic positions:

$$x_i^\alpha(t+\Delta t) = x_i^\alpha(t) + \dot{x}_i^\alpha(t)\Delta t + \frac{1}{2}\ddot{x}_i^\alpha \Delta t^2 + \frac{1}{6}\dddot{x}_i^\alpha \Delta t^3 + O(\Delta t^4) \tag{2.3a}$$

$$x_i^\alpha(t-\Delta t) = x_i^\alpha(t) - \dot{x}_i^\alpha(t)\Delta t + \frac{1}{2}\ddot{x}_i^\alpha \Delta t^2 - \frac{1}{6}\dddot{x}_i^\alpha \Delta t^3 + O(\Delta t^4) \tag{2.3b}$$

adding the above equations gives:

$$x_i^\alpha(t+\Delta t) = 2x_i^\alpha(t) - x_i^\alpha(t-\Delta t) + \ddot{x}_i^\alpha \Delta t^2 + O(\Delta t^4) \tag{2.4}$$

substituting the expression from Newton's second law (2.2) results in:

$$x_i^\alpha(t+\Delta t) = 2x_i^\alpha(t) - x_i^\alpha(t-\Delta t) + \frac{F_i^\alpha}{m_i}\Delta t^2 + O(\Delta t^4) \tag{2.5}$$

It is clear from (2.5) that the atomic positions may be calculated without knowledge of the atomic velocities; however, the total energy of the system includes a kinetic

contribution, which requires the atomic velocities to be known. In the Verlet method, the velocities are calculated by implementing a first-order central difference calculation:

$$\dot{x}_i^\alpha = \frac{x_i^\alpha(t+\Delta t) - x_i^\alpha(t-\Delta t)}{2\Delta t} \tag{2.6}$$

To perform MD simulations that realistically model material behavior, an appropriate timestep Δt must be chosen. The characteristic timestep for a system of atoms is dependent on the specific properties of the system being modeled. For all of the MD simulations performed in this work, we have chosen a timestep of 1 femtosecond, which is sufficiently within the characteristic timestep for the material systems considered.

The MD simulations in this work are performed within an *NVT* ensemble. In this type of calculation, the number of atoms in the system *N*, the volume *V*, and the temperature *T* are held constant. The temperature is maintained through the use of a Nosé-Hoover thermostat.[41, 42] For a detailed discussion on the theoretical basis for MD ensembles and the Nosé-Hoover thermostat, the reader is referred to the text by Frenkel and Smit.[43]

2.4 Embedded-atom method potential

The EAM was developed by Daw and Baskes [28, 44] to calculate the equilibrium properties of metallic systems. The EAM is an extension of the quasiatom and effective medium theories[45, 46], in which unlike a pure pair-potential, the energy of an atom is dependent on the local binding environment. Since the functional form of the total system energy in the EAM is dependent on the local binding environment, it is well

suited for capturing the effects of free surfaces in nanometer scale materials. In the EAM, the total energy U of a system of N atoms is a summation over two terms, a classical pair interaction and a many-body, embedding energy term and is given as

$$U = \sum_{i}^{N} \left(F_i(\bar{\rho}_i) + \frac{1}{2} \sum_{\substack{i,j \\ i \neq j}}^{N} \phi_{ij}(R_{ij}) \right) \tag{2.7}$$

where, F_i is the energy required to embed an atom into the background electron density $\bar{\rho}_i$ at position i and ϕ_{ij} is the short-range pair interaction between atoms i and j separated by a distance R_{ij}. In the EAM the electron density does not include an angular dependence, therefore use of this method is restricted to material systems in which there is minimal directionality of primary bonds, such as is the case for many FCC metals. It should be noted that an extension to the EAM has been developed, the modified embedded-atom method (MEAM)[47-50], for materials systems that exhibit directionally dependent bonds; however, this method is not used in the current work.

The simulations in this work were performed using the EAM potential for silver developed by Voter and Chen.[51] This potential was fit to experimentally determined properties of silver, as presented in Table 2.1, following. For atomistic simulations in which the mechanical behavior is probed beyond the elastic regime, it has been shown that in addition to the parameters provided in Table 2.1, the chosen interatomic potential must accurately capture the unstable and intrinsic stacking fault energies of the material system. While the Voter and Chen EAM potential is not directly fit to these quantities, the potential is able to reproduce these quantities within acceptable error. A more in-

depth discussion on the calculation of stacking fault energies from atomistic simulations is presented in Section 2.7.

Table 2.1: Fitting parameters of the Voter and Chen EAM potential as compared to the experimental values for silver. The parameters are: equilibrium lattice constant (a_0), bulk cohesive energy (E_{coh}), bulk modulus (B), cubic elastic constants (C_{11}, C_{12}, C_{44}), vacancy formation energy (ΔE_{vf}), diatomic molecule bond strength (D_e), and diatomic molecule bond length (R_e).

Property	Experimental	Voter and Chen
a_0 (Å)	4.09	4.09
E_{coh} (eV)	2.85	2.85
B (10^{12} erg cm^{-3})	1.04	1.04
C_{11} (10^{12} erg cm^{-3})	1.24	1.24
C_{12} (10^{12} erg cm^{-3})	0.934	0.93
C_{44} (10^{12} erg cm^{-3})	0.461	0.46
ΔE_{vf} (eV)	1.1	1.10
D_e (eV)	1.66	1.66
R_e (Å)	2.5	2.50

Data reproduced from [51]

2.5 Simulation boundary conditions

In atomistic simulations, typically, a global simulation box is established which contains all atoms in the simulation. The 'box' occupies a defined volume in coordinate space and all atomistic calculations are restricted to this space. The edges of the simulation box may be assigned one of two boundary conditions according to the type of simulation being performed, *periodic* or *non-periodic*, and these conditions may be applied in each of the primary directions, orthogonal to the box edges. When periodic boundary conditions are imposed, atoms located at the boundaries of the simulation box are considered to experience an external (to the simulation box) binding environment that mirrors the binding environment on the interior of the simulation box. In simulations where a group of atoms is being considered as a representative section of a continuous

(bulk) material, the boundary conditions on the global simulation box are periodic in all directions, and the simulation is said to be *fully periodic*. If periodic boundary conditions are only specified in two directions, then the simulation represents a 'sheet' of atoms of finite thickness and infinite span, with free surfaces bounding the directions that are *not* periodic. When periodicity is specified in only one direction, a 'rod' of atoms is represented of infinite length but with a finite cross-sectional geometry. The simulations in this work do not contain periodic boundary conditions in *any* direction, thus each outermost plane of atoms is a *free surface*, and the atoms comprising the simulation may be considered to be a freestanding structure.

2.6 Application of atomistic simulations

In this section, the application of MS and MD in this work will be outlined. The general simulation procedures will be presented in a broad context. The role of MS and MD simulations in capturing the mechanical response of metal nanowires is explained. The specific simulation procedures are reserved for the 'methods' section of each chapter.

2.6.1 Atomistic simulation precursors

Each atomistic simulation begins with the specification of the positions of all atoms in the system. Atomic positions are specified by *x*,*y*, and *z* Cartesian coordinates, according to the crystallographic characteristics of the system being modeled. For monocrystalline nanowires, the structure of the nanowire 'specimen' is defined by the crystallographic axial orientation of the nanowire axis and of the nanowire free surfaces. In each atomistic simulation contained in this work, the initial atomic coordinates are

dictated by the crystallographic characteristics of the specific nanowire geometry being represented, in accordance with the properties of the bulk lattice.

As previously discussed in Chapter 1, atoms at or near the surface of a nanometer scale structure will contract towards the interior of the structure in order to maximize their local electron-density, while concurrently minimizing the excess energy resulting from under-coordination at the free surface. Since the initial atomic coordinates in each simulation are corresponding to the bulk positions, this surface contraction is not initially captured, and the structure being considered is not in a minimum energy, equilibrium state. In order to capture this surface contraction, all atomistic simulations begin with an energy minimization, MS step.

2.6.2 Energetics of mechanical deformation

When mechanical deformation is imposed on a system of atoms, the total energy of the system is increased. In Figure 2.1, a schematic of the potential energy for a hypothetical material system is plotted against an atomic configuration parameter. In this schematic, various states of equilibrium are apparent. The atomic configurations at states 'A' and 'D' may be considered to be at *stable* equilibrium, since they are both in a state of minimum energy (in the local sense). Atomic configuration 'C' exists at a 'saddle-point' on the potential energy surface and is said to be in a state of *unstable* equilibrium. Finally, atomic configuration 'B' is at an intermediate state between *stable* and *unstable* equilibrium. This schematic may be used to understand the energetics of mechanical deformation in an atomistic simulation. Configuration 'A' is the atomic configuration after the initial MS energy minimization. If mechanical work is performed on the system of atoms, the configuration will transition from 'A' up the potential energy curve, to an

intermediate configuration at ‘B’, until the saddle-point at ‘C’ is reached. At configuration ‘C’, upon further mechanical deformation, the accumulated mechanical energy is alleviated through the nucleation and propagation of defects in the system. After the defects are nucleated, and have propagated through the structure, a second point of stable equilibrium is reached, represented by configuration ‘D’. Thus it may be stated that the deformation up to configuration ‘C’ is elastic in nature, and that if the load were removed before reaching the saddle-point configuration, the system would return to the stable equilibrium configuration of ‘A’. Upon reaching configuration ‘D’, irreversible work has been performed on the system, and the deformation is inelastic (plastic) in nature.

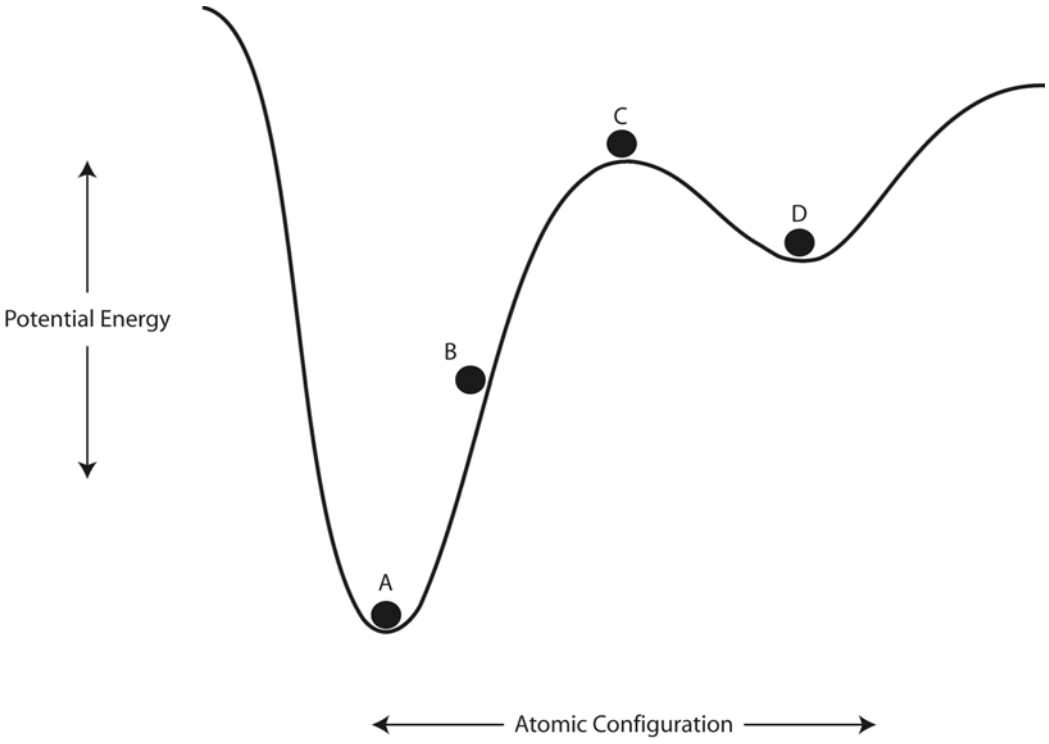

Figure 2.1: Schematic of the potential energy of a materials system for various atomic configurations.

In this work, both MS and MD calculations are utilized to analyze the mechanical response of metal nanowires. While all simulations begin with a MS energy minimization step, whether MS or MD is used for the remainder of the atomistic simulation is determined by which deformation regime is being probed: elastic or inelastic. MS calculations are unable to capture saddle-point configurations, since the conjugate gradient method follows the direction of steepest *decent*. For this reason, MS calculations are used to infer the elastic response of nanowires, much below the saddle-point of the potential energy curve. MD calculations are used in instances where knowledge of the atomic configurations near the saddle point are desired, such as during the nucleation of defects (yielding) of nanowires.

2.6.3 General loading procedures

In the atomistic simulations presented in this work, two general procedures are used to apply mechanical deformation. In MS calculations, since time is not a parameter, mechanical deformation is implemented through displacements of the atoms according to a prescribed trajectory. In MD simulations, deformation is implemented by prescribing a velocity to the atoms, again, along a prescribed path.

2.6.3.1 Molecular statics loading procedure

In MS, mechanical deformation is achieved through the application of displacements to the atoms in the system. For the simple case of the tensile deformation of a nanowire, the loading procedure is summarized below.

1) the atomic positions of a set of atoms at one end (fixed-end) of the nanowire are constrained by imposing a zero-force boundary condition

2) the atoms in the nanowire are displaced according to a linear displacement gradient, where the displacements range from zero at the fixed-end, to a maximum value at the free end
3) atoms at both ends of the nanowire are constrained with a zero-force boundary condition
4) MS energy minimization is performed to obtain the strained atomic configuration, and to provide the potential energy of the system

In the above procedure, the maximum displacement must be small in order to maintain stability in the atomistic simulation. This results in a 'incremental' loading procedure, where steps (2) – (4) are repeated until a desired, maximum strain is reached in the nanowire. In the MS simulations in this work, 0.2% strain is applied per increment of loading. The zero-force boundary conditions are necessary to assure that the nanowire retains its strained configuration during energy minimization. If this boundary condition were not imposed, the nanowire would relax back to its initial minimum energy configuration after each loading increment.

2.6.3.2 Molecular dynamics loading procedure

The loading procedure for MD simulations is dynamic in nature, and is achieved through the application of velocities to the atoms in the material system. The general loading procedure for the dynamic tensile deformation of a nanowire is outlined below.

1) the atomic positions of a set of atoms at one end (fixed-end) of the nanowire are constrained by imposing a zero-force boundary condition

2) velocities are prescribed in the axial direction of the nanowire according to a linear profile, where the velocity varies from zero at the fixed-end to a maximum value at the free-end

This loading procedure results in the tensile deformation of the nanowire at a constant strain rate, and is referred to as a continuous, dynamic loading procedure. For the MD simulations in this work that utilize this procedure, the strain rate is 10^8 s^{-1}.

2.7 Stacking fault energy in atomistic simulations

In a perfect FCC crystal, the close-packed planes are arranged such that an 'ABC' stacking order exists in the material. When the material is subjected to a mechanical force, beyond the elastic limit, dislocations are generated which alleviate the mechanical work on the system by rearranging the atomic order in the system. The energetic change during this process was illustrated previously (in a hypothetical sense) in Figure 2.1, as the change in potential energy (and atomic configuration) from state 'C' to state 'D'. The motion of dislocations produces plastic deformation in the material. Generally speaking, two 'types' of dislocations may be generated in a material. These are full dislocations and partial dislocations. When a full dislocation is nucleated and propagates through a material along a close-packed plane, the {111} planes on either side of the dislocation slide past one another for a distance equivalent to one full burger's vector, and the stacking of the {111} planes remains in the 'ABCABC' configuration. When the dislocation exits the crystal at a free surface, a surface-step is produced. In nanometer scale materials, this type of dislocation is often not energetically favorable, because the excess energy created by a surface step is large. For nanometer scale materials, partial dislocations are more frequently observed. When partial dislocations propagate through a

FCC material, they disrupt the stacking order of the lattice from ABCABC to ABABCA, the disrupted stacking order is referred to as a *stacking fault*.

In order to generate a stacking fault in a crystalline material, an energetic barrier must be overcome. This energetic barrier is the unstable stacking fault energy $\gamma_{usf.}$ After the unstable-stacking fault energy has been reached, a stacking fault is formed, and the energy decreases to the intrinsic stacking fault energy γ_{isf}. In atomistic simulations that probe the mechanical response into the plastic regime, it has been demonstrated that the ability of the interatomic potential to reproduce these energetic parameters is essential.[52-54] As previously stated, the Voter and Chen EAM potential was not directly fit to the experimental values of the unstable and intrinsic stacking fault energies. In order to assess the capability of this potential to model the plastic deformation of silver nanowires, it is necessary to generate a generalized stacking fault curve and compare the calculated stacking fault energies to published experimental and *ab initio* values.

2.7.1 Calculation of generalized stacking fault curves

The generalized stacking fault (GSF) curve summarizes the energetic landscape during the process of first creating an intrinsic stacking fault, and then creating an extrinsic stacking fault (twin fault) in an FCC crystal. During this process, which is visually presented in Figure 2.2, an atomistic simulation box is constructed, in which the edges of the box are perpendicular to the <111>, <110>, and <112> directions. The simulation is periodic in the <110> and the <112> directions, thus an infinite slab of atoms are modeled. The block of atoms being modeled is then divided into two halves (an upper and a lower portion), along the <111> direction. To create a stacking fault in the crystal, the lower block of atoms is constrained, and the upper half is displaced along

the <11-2> direction, in small increments. After each incremental displacement, the position of all atoms in the crystal are fixed in the <11-2> and <110> direction, and the system is allowed to relax freely in the <111> direction. Next, an energy minimization MS step is performed in order to calculate the total energy of the system. This process is repeated for several displacements along the <112> direction, until the atomic configurations corresponding to those in Figure 2.3 are reached. It is noted that once an intrinsic stacking fault is created, the planes that comprise the stacking fault become a part of the lower block of atoms (which remains fixed during the displacement process). This results in the generation of a twin fault in the crystal. The energy data accumulated during the displacement process is then plotted versus the displacement along the <112> direction to generate the GSF curve. The GSF curve generated from the Voter and Chen EAM potential for silver is presented below in Figure 2.3.

Also included in Figure 2.3, are an experimental data point for the intrinsic stacking fault energy, and data points for each maxima and minima, obtained from *ab initio* tight-binding calculations. It is apparent that the Voter and Chen EAM potential for silver compares well with these published values, and thus accurately reproduces the stacking fault energies necessary to adequately model plastic deformation in an atomistic simulation.

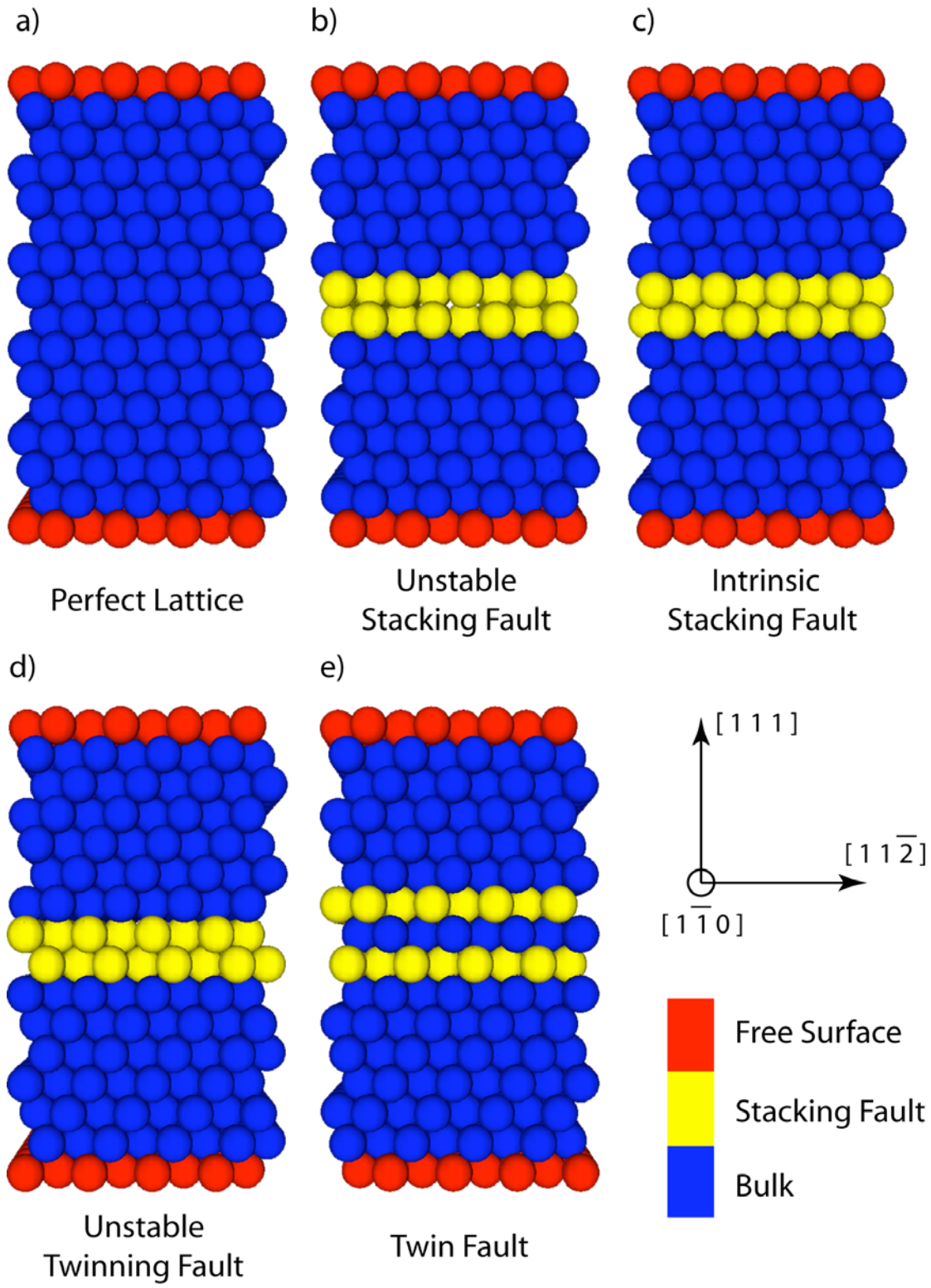

Figure 2.2: Atomic configurations obtained during the calculation of a generalized stacking fault curve.

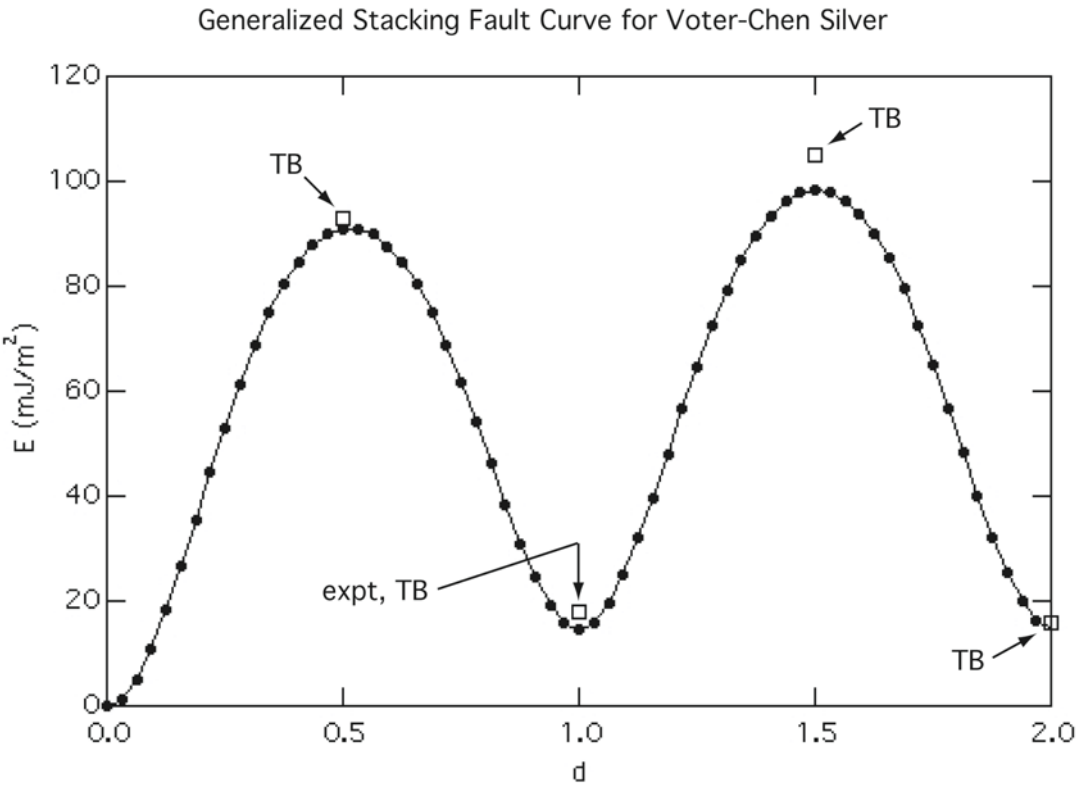

Figure 2.3: Generalized stacking fault curve for the Voter-Chen silver EAM potential. The energy is plotted against the fractional displacement along the <112> direction, where $d = 0.0$ is a perfect lattice, $d = 0.5$ is the position of the unstable stacking fault, $d = 1.0$ is the intrinsic stacking fault, the unstable twin fault is at $d = 1.5$, and the extrinsic stacking fault is at $d = 2.0$. Data from tight binding (TB) calculations (γ_{usf}, γ_{isf}, γ_{ut}, γ_{esf}) and experimental measurements (γ_{isf}) [55, 56] are presented for comparison.

CHAPTER III

TENSILE DEFORMATION OF *TOP-DOWN* AND *BOTTOM-UP* NANOWIRES

3.1 Introduction

Nanowires are discernable by the geometry of their cross sections. In turn, this geometry is a manifestation of how the nanowires were created and the mechanisms by which the wires attained a state of minimum free energy. In general, nanowires may be separated into two classes based on the method of fabrication: *top-down* and *bottom-up*. *Top-down* methods involve extraction of a nanowire from a bulk sample through processes such as electron beam lithography or mechanical reduction [16, 57-59], while *bottom-up* classifies nanowires that have been grown through chemical or molecular assembly or by template assisted electrodeposition [17-25]. For further information on these processes, the reader is referred to thorough reviews of current methodologies for the fabrication of one-dimensional nanostructures [3, 60, 61].

When subjected to an applied stress, bulk and nanometer scale materials exhibit fundamentally different mechanical responses. For instance, consider the tensile behavior of monolithic metals (single crystal and unalloyed) at two different length scales portrayed in Figure 3.1. Bulk material mechanical response is typified by linear-elastic deformation followed by yield and subsequent plastic flow, generally not exceeding the MPa range [62]. However, at nanometer scales, strengths in the GPa range are attainable and the overall response is characterized by a series of discrete yielding events leading to

fracture [27, 63, 64]. The quantized nature of deformation at the nanometer scale reveals a disparity in the loading method. If the applied tensile stress is incrementally increased during deformation (force control), the mechanical response exhibits instabilities in strain corresponding to 'instantaneous' changes in specimen length due to the motion of internal defects. Conversely, applying an incrementally increasing strain (displacement control) reveals yielding in increments of force (stress) instability attributable to dissipation of stored strain energy through the nucleation and motion of internal defects.

The complexities associated with experimental measurements of the mechanical properties of nanometer scale materials preclude conventional testing methods and lend towards computational tools to simulate the mechanical behavior using atomistic

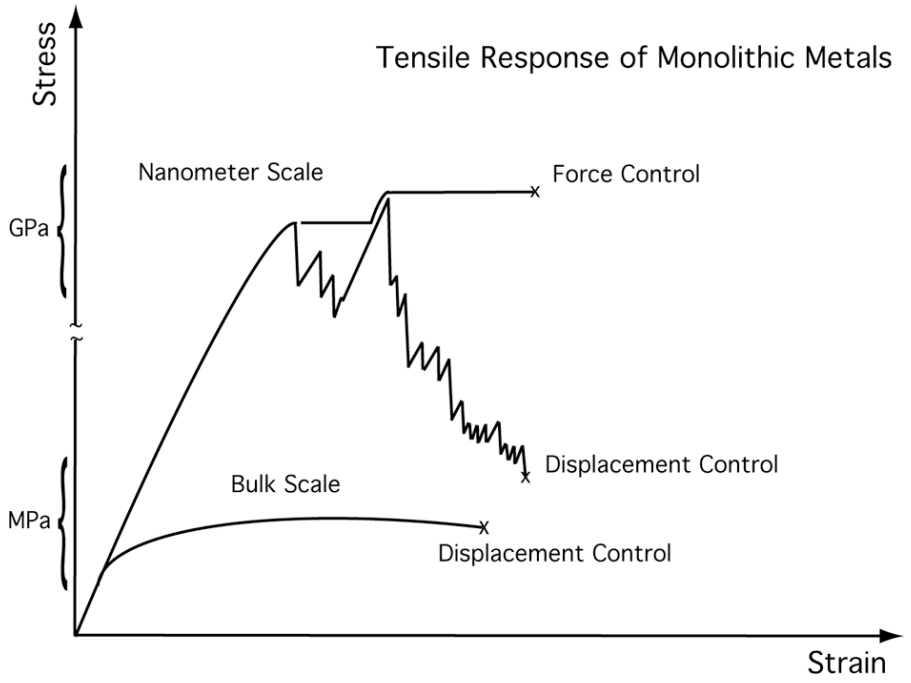

Figure 3.1: Schematic of the mechanical response of bulk and nanometer scale monolithic metals under force and displacement controlled tensile loading.

simulations, specifically, molecular dynamics (MD). MD simulations using the embedded atom method (EAM) have provided a fundamental understanding of the mechanical behavior of nanowires [32, 34, 35, 39, 52, 65-74].

In particular, nanowires of face-centered-cubic (FCC) metals have been studied extensively. Simulations of gold nanowires [65] have shown that surface-stress resulting from excess energy at free surfaces can be sufficient to induce a phase transformation from FCC to body-centered-tetragonal if the wire cross-section is reduced to a critical dimension. Recently it has been demonstrated that surface stresses may also facilitate reversible lattice reorientations in some FCC nanowires, leading to shape-memory and pseudoelastic behavior [70-74]. In general, single crystal metallic nanowires are predicted to deform by two deformation mechanisms, twinning and partial dislocation motion (slip) [39]. It has been shown that the initial deformation mechanism is dependent not only on the nanowire axial and free surface orientations (in relation to the loading direction), but also on the predictive capacity of the atomistic model with respect to the unstable and intrinsic stacking-fault energies [52, 54].

Thus far, MD simulations of the deformation of metallic nanowires have primarily focused on wire geometries that are inherently unstable due to high-energy surface and axial orientations. A notable exception is the recent work by Hyde *et al.* [35] on single-crystal gold nanowire structures; this study investigates the mechanical properties of stable <110> and <111> axial orientations, but considers the more hypothetical, circular cross-sectional geometries rather than experimentally observed nanowire geometries (which are typically faceted). While these investigations have been crucial in formulating an initial understanding of nanowire mechanical behavior, the

scope of their practical application to the structural integrity of nanometer scale devices may be limited as the simulated nanowire configurations are mostly theoretical. We also note that the mechanical response of nanowires with a rhombic cross-section has been previously considered [39, 66, 70-74]. However, these studies have focused primarily on reversible deformation paths which lead to shape memory and pseudoelastic behavior. The deformation behavior of the truncated-rhombic nanowires, to the author's knowledge, has not been considered.

We consider <110> axially oriented silver nanowires of rhombic and truncated-rhombic geometries, representative of *top-down* fabrication; and also the multiply twinned, pentagonal geometry typifying a *bottom-up* fabrication route. The rhombic structure was first observed in high-resolution transmission electron microscopy (HRTEM) by Kondo and Takayanagi [16] and later by Kizuka [75] and Rodrigues *et al.* [76] in gold nanowires created from electron-beam irradiation of thin films. The cross-sectional geometry is a result of the crystallography of four low-energy {111} side surfaces that join to form a rhombus. A truncation of the acute vertices of the rhombic nanowires results in the exposure of {100} surfaces along the nanowire length and a truncated-rhombic geometry. The truncated-rhombic nanowires are predicted to be energetically more favorable than the rhombic structure [77] and have been specifically observed during *in-situ* HRTEM observation of *top-down* nanowire fabrication in silver [78, 79]. The pentagonal geometry is a stable structure produced by chemical growth using techniques utilized by Caswell *et al.* [17] as well as Sun and Xia [23] for silver nanowires. The pentagonal nanowire structure has been extensively characterized using electron microscopy and electron diffraction [19, 80-84], but the deformation behavior has not been

investigated using MD, particularly in the case of silver. An excellent discussion of the energetics and relative stability of the three nanowires is found in the work by Tommei *et al.* [77].

In this study, we present a detailed analysis of the mechanical behavior of experimentally observed, inherently stable *top-down* and *bottom-up* silver nanowires. We probe the mechanical behavior of the nanowires under tension from an equilibrium configuration until failure with specific emphasis on the mechanisms of initial yield. We consider nanowires ranging from 1 – 25 nanometers in diameter (up to two million atoms). The consideration of large nanowires broadens the scope of the research to more commonly observed and fabricated nanowire sizes. We show that the method of fabrication *(top-down vs. bottom-up*) has a direct influence on the mechanical behavior of metallic nanowires. While we only simulate the deformation of silver nanowires, nanowires fabricated from other low stacking-fault energy metals such as gold and copper are expected to show similar behavior. We illustrate that *top-down* and *bottom-up* nanowire structures demonstrate fundamentally different deformation mechanisms and dissimilar overall mechanical behavior.

Our results also indicate a strong, geometry dependent size effect on the tensile yield strength. Several researchers have described a size effect in the elastic properties of nanometer scale materials, in experiments [85-88], continuum based models [89-93], and atomistic simulations [67, 94]. In all cases, the variation of the elastic properties is attributable to the increasing influence of surfaces as the dimensions of the structure are reduced. In this sense, our findings reaffirm the former conclusion, that the excess energy of free surfaces has a significant influence on the mechanical behavior of

nanowires; however, our results are distinct in that we observe the size effect in the plastic regime. Furthermore, we demonstrate that in relation to the bulk mechanical properties, the magnitude of the size effect is different for nanowires of the same material and axial orientation but of varying geometry.

This chapter is organized in the following manner. We first present an overview of the tensile deformation from zero strain to failure including a thorough discussion of the initial defect nucleation, for each nanowire geometry. We then offer conclusions on the mechanical behavior of metallic nanowires. Lastly, the methods employed to simulate the deformation of the silver nanowires are described and a detailed presentation of the crystallographic structure of the three considered geometries is provided.

3.2 Simulation Methodology

Experimentally observed silver nanowires representative of *top-down* and *bottom-up* fabrication were considered for the analysis. Three nanowire geometries were modeled, each of a <110> axial orientation. The three-nanowire structures are presented in Figure 10. The *top-down* nanowires exhibit rhombic (Figure 3.2a) and truncated-rhombic (Figure 3.2b) cross-sections, while the *bottom-up* structure exhibits a pentagonal (Figure 3.2c) cross-section. The three wires will be referred to as rhombic, truncated-rhombic, and pentagonal. The rhombic and truncated-rhombic nanowires are each single crystal, while the pentagonal nanowire is comprised of five wedge-shaped single crystals (each with a <110> fiber texture) arranged in a pentagonal geometry.

The nanowires are created with atoms in positions corresponding to a bulk FCC crystal lattice. We do not consider periodic boundary conditions in any direction for the nanowires, thus atoms in proximity to free surfaces will have a tendency to contract in

order to increase their effective electron density and thus decrease the energy of the system. To facilitate this contraction, the precursor to all simulations is conjugate gradient energy minimization. The nanowires are then dynamically equilibrated at 300 K using a Nosé-Hoover thermostat [41, 42] for 100 ps. Free boundary conditions are prescribed during the dynamic equilibration to allow thermal expansion so that a stress-equilibrated state is maintained in the nanowire. The final step is to apply a tensile, displacement-controlled load to the nanowire until failure occurs. For this, two techniques are used: continuous dynamic and incremental dynamic loading.

In the continuous dynamic loading method, atoms in the nanowire are assigned a velocity in the axial, <110> direction according to a linearly varying velocity profile along the length of the nanowire. The velocity varies from zero at the fixed end of the nanowire to a maximum value at the free, resulting in a strain rate of 1×10^{8} s^{-1}. This velocity profile mitigates loading-induced shock waves that are characteristic of a uniform velocity profile in MD simulations. While this strain rate is quite large in a classical sense, it is typical of MD simulations and is sufficiently below the strain rate at which precludes dislocation motion, which occurs on an extremely quick timeframe [69].

The incremental dynamic approach consists of a series of incremental displacements, during which each atom in the nanowire is displaced according to a linear profile. In the elastic regime (prior to permanent deformation), the nanowire is strained 0.45% of its length per increment, corresponding to approximately 10% of the yield strain per increment. Large displacements are allowable during elastic deformation, since the material response is expected to be linear. As the elastic limit is approached, the displacements are reduced to 0.1% strain per increment. After each displacement, the

ends of the wire are constrained from axial motion and the wire is dynamically equilibrated at 300 K for 100 ps. This incremental dynamic approach results in an effective strain rate of $1x10^{7}$ s^{-7}. During the equilibration, the axial stress saturates to a nearly constant value; this value is determined as a direct average of the stress over the latter 50 ps of equilibration. In both loading methods, the virial theorem is used for stress calculations and is averaged over the instantaneous *physical* volume of the nanowire [95, 96].

The detailed investigations of the deformation mechanisms for each nanowire (as presented in Figures 3.5, 3.7, and 3.9) were performed at 10K in order to reduce the contribution of thermal oscillations to the centrosymmetry values of the atoms. The continuous dynamic loading method was utilized at a strain rate of $1x10^{8}$ s^{-1} for these simulations. No change in deformation mechanism was observed between the simulations at 10K and 300K.

We also performed simulations on the three geometries with diameters ranging from one to around twenty-five nanometers in order to investigate the effect of nanowire size on the tensile yield strength. For these simulations, where in some cases the system size exceeds 10^{6} atoms, the continuous dynamic loading method was employed with a strain rate of $1x10^{9}$ s^{-1}. Snapshots of the large nanowires after yield were observed to verify that no change in mechanism occurred. The dimensions and relative stability of all of the nanowires considered in this work are summarized in Table 3.1.

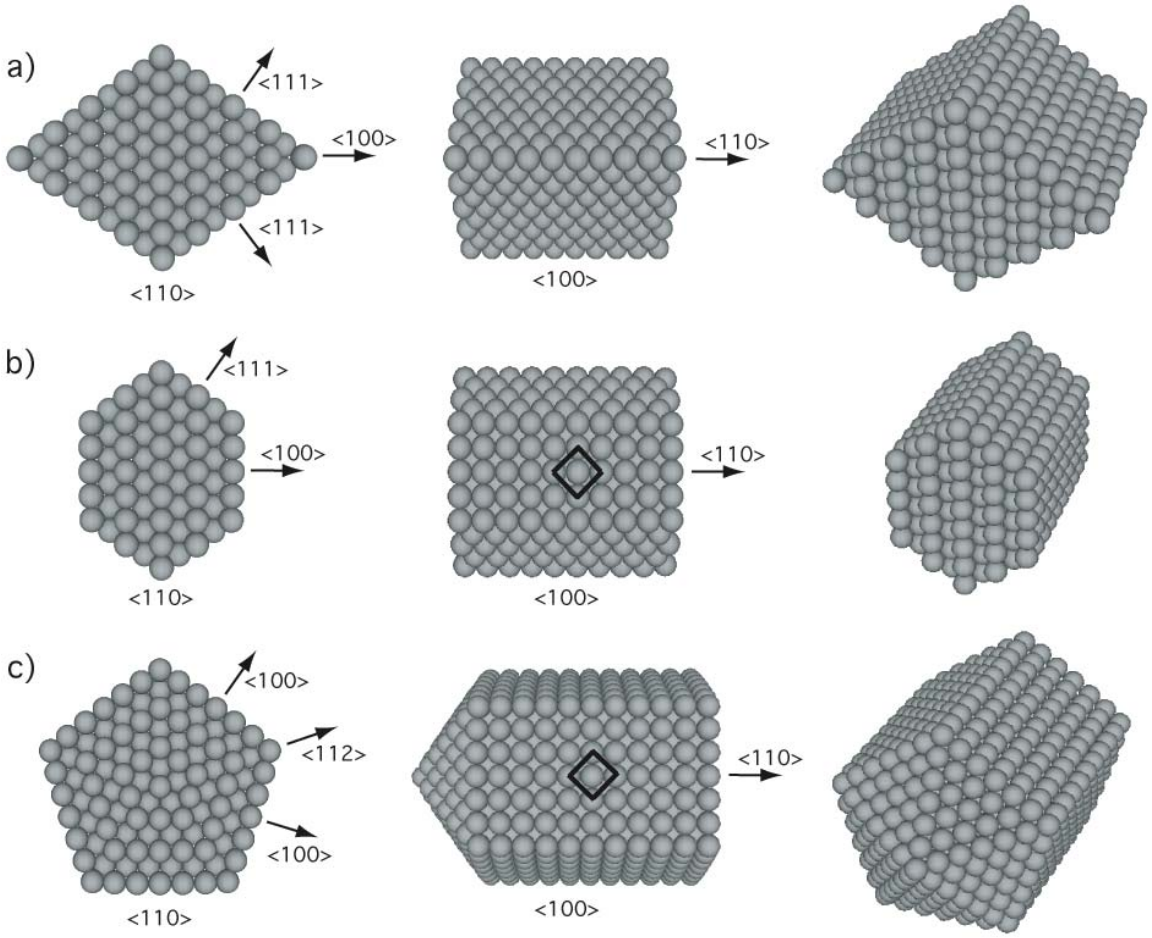

Figure 3.2: *Top-down* (a, b) and *bottom-up* (c) silver nanowires. Three views are shown for each wire type: cross-section (left), side view (middle), and three-dimensional perspective (right). The viewing direction is indicated below each image (left, middle). All wires have an FCC structure and are axially oriented in the <110> direction. The *top-down* nanowires have a rhombic (a) or truncated-rhombic (b) cross section. The rhombic wires have {111} type lateral surfaces while the truncated-rhombic wires reveal {100} facets in addition to the {111} surfaces. The pentagonal nanowire (c) is representative of *bottom-up* fabrication, and may be considered as a multiply twinned nanowire. Five wedge shaped rods are separated by {111} twin boundaries along the nanowire length, and are arranged in a pentagonal geometry. The lateral surfaces of the pentagonal wire are of a {100} orientation, while the wire-ends expose low-energy, close-packed {111} facets.

Table 3.1: Geometric parameters and relative stability of the simulated nanowires. The nanowire diameter (D) is the diameter of a circle with a cross sectional area equivalent to that of the nanowire being considered. The ratio of the nanowire length to the diameter was approximately 8 for all nanowires except the largest diameter of each geometry. For the large diameters, the aspect ratio was decreased to reduce the number of atoms in the system (N_A). The cohesive energy (E_{coh}) is a per-atom quantity and is a measure of the energetic stability of the nanowires. The nanowire configurations that are considered in detail are shown in bold.

Geometry	D (nm)	N_A	E_{coh} / E_{bulk}
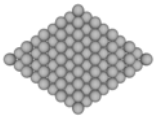 Rhombic	1.10	838	0.892
	2.20	**4,982**	**0.940**
	4.39	33,669	0.968
	7.13	135,229	0.980
	12.07	626,737	0.988
	21.95	2,030,629	0.993
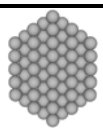 Truncated-Rhombic	0.95	638	0.881
	1.90	**3,754**	**0.934**
	3.80	25,285	0.965
	6.18	96,282	0.977
	10.46	470,142	0.987
	19.01	1,471,694	0.992
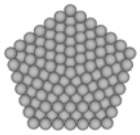 Pentagonal	1.70	1,584	0.921
	2.56	**6,117**	**0.946**
	6.02	64,883	0.976
	8.61	181,136	0.983
	14.67	854,135	0.990
	26.79	2,034,625	0.994

3.3 Results

The tensile stress-strain response of the rhombic, truncated-rhombic, and pentagonal nanowires is presented in Figure 3.3. The response is provided from zero-strain to failure for each nanowire. The three-nanowire geometries show similar mechanical behavior up to the onset of plastic deformation, characterized by an initial nonlinear elastic response. However, after the primary defect nucleation event, the mechanical response of the three nanowires is fundamentally different; each undergoing

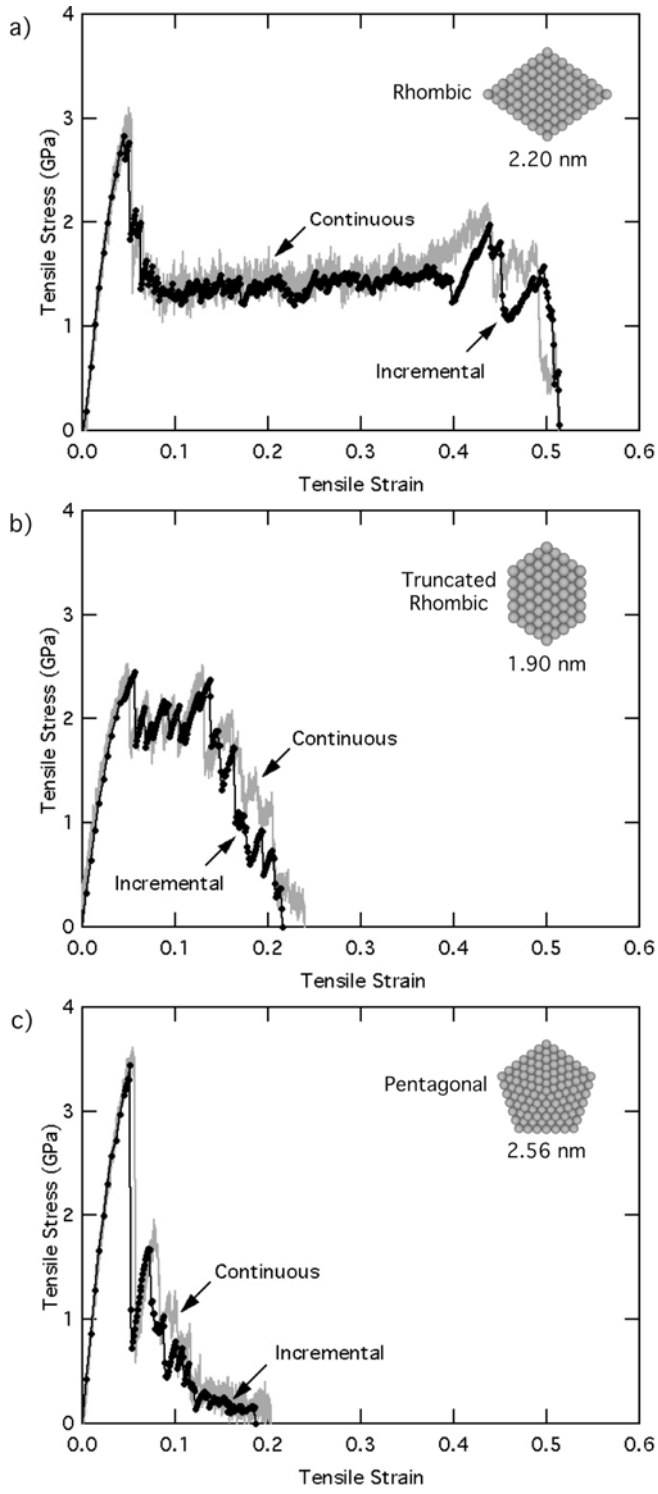

Figure 3.3: Stress-strain response of *top-down* (a,b) and *bottom-up* (c) silver nanowires. The nanowire geometry and diameter are indicated for each response. The wires were loaded in tension from an unstrained, thermally equilibrated (300 K) configuration to failure. The stress shown is the virial stress.

deformation by means of a different mechanism leading to vastly different failure strains. In the following, we provide a detailed presentation of the mechanical response of the three nanowires. Snapshots representative of the dominant stages of overall deformation for each nanowire are provided with a particular focus on the mechanisms surrounding initial yield.

3.3.1 *Top-Down* Rhombic Silver Nanowires

The mechanical response of a rhombic silver nanowire is presented in Figure 3.3a. Snapshots of the nanowire at consecutive stages of deformation are shown in Figure 3.4. The defect free, minimum energy configuration (Figure 3.4a) sustains an axial stress of approximately 3 GPa before partial dislocations of the Shockley type are heterogeneously nucleated at the intersection of two {111} free surfaces, resulting in the formation of an intrinsic stacking fault in the FCC lattice. The nanowire then undergoes deformation twinning, where coherent twin boundaries are propagated from the initial stacking fault to the nanowire ends (Figure 3.4b-c). During this process, the wire undergoes an axial lattice reorientation from <110> to <100> resulting in the conversion of the low-energy {111} free surfaces to higher-energy {100} surfaces. As a direct consequence of the free surface orientation, the cross-sectional geometry transitions from rhombic to rectangular during the twinning process. The nanowire expands an extraordinary amount, over 40% of its original length during the reorientation. The reoriented <100> nanowire is essentially defect-free; the twin boundaries are pinned at the free ends due to the imposed boundary conditions. The <100> nanowire then behaves elastically followed by yield through the nucleation and motion of additional Shockley partial dislocations (Figure

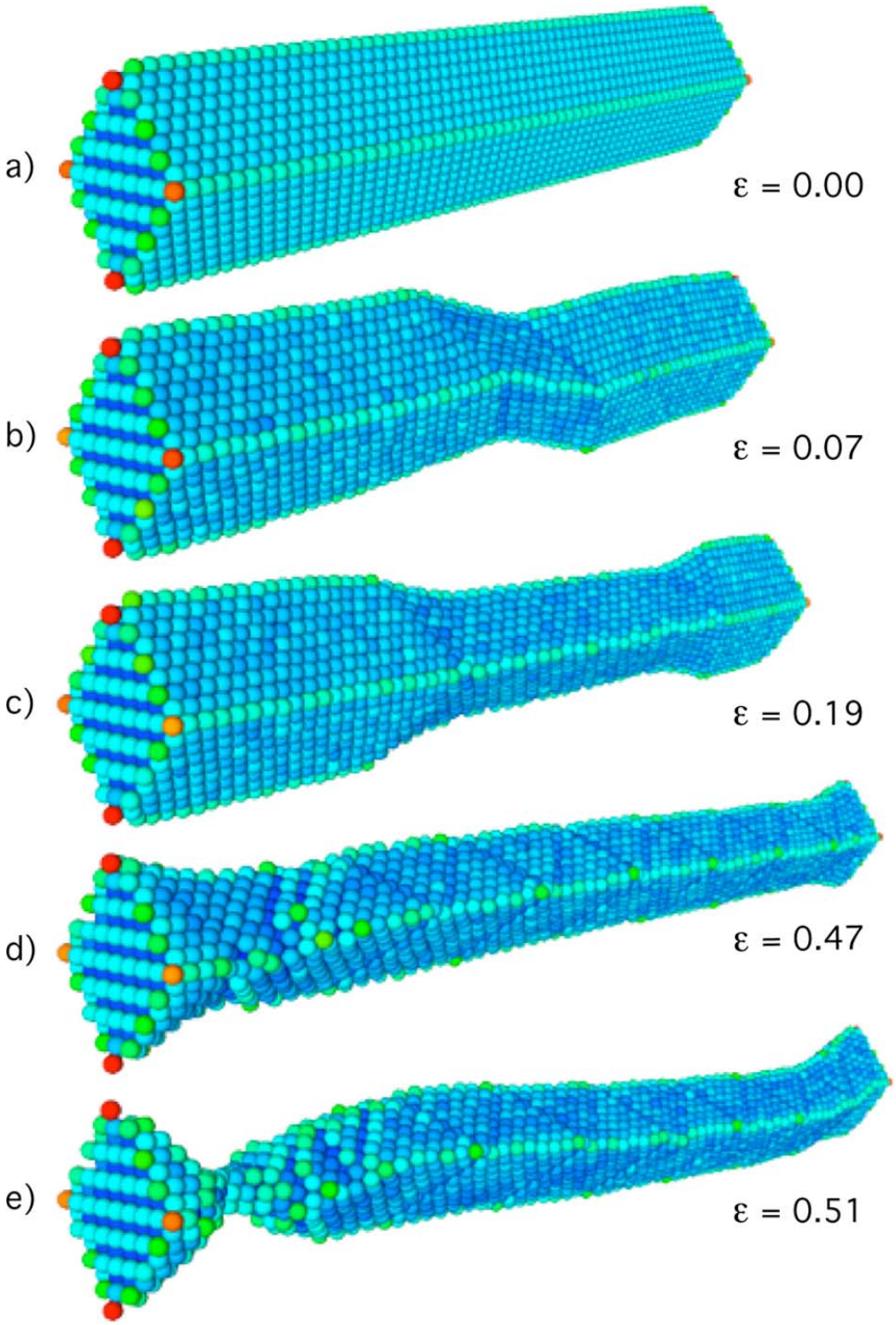

Figure 3.4: Snapshots of a rhombic silver nanowire during tensile deformation at 300 K. The strain value for each snapshot is indicated and corresponds to the stress-strain response in Figure 3.3a.

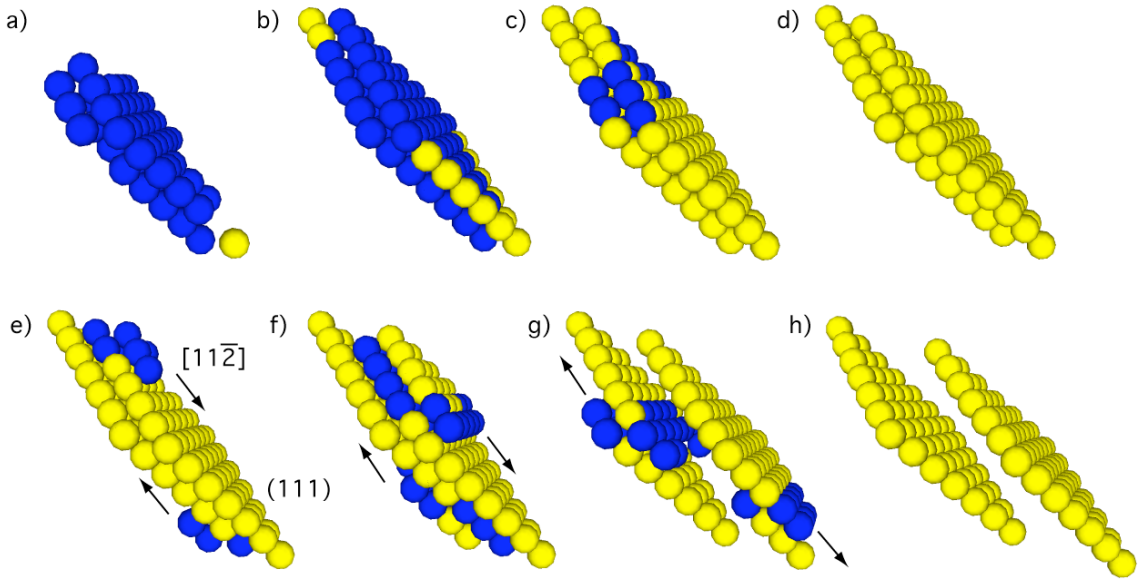

Figure 3.5: Stacking fault formation (a-d) and twin propagation (e-h) in a rhombic silver nanowire subjected to tensile deformation at 10 K. Atoms are colored by a centrosymmetry parameter indicating the degree of coordination for each atom relative to its undisturbed (bulk) position. Blue atoms correspond to partial dislocations while yellow atoms are representative of stacking fault coordination. Fully coordinated atoms are not shown. Arrows are shown indicating the direction of partial dislocation motion during the propagation of the twin boundaries.

3.4d). The plastic flow is restricted as the partials form a network of Lomer-Cottrell locks along the nanowire length. Finally, the nanowire deforms into a helically arranged cylindrical structure as the cross-section is reduced through necking (Figure 3.4e), eventually leading to the formation of a single atomic strand just prior to failure.

The initial decrease in strength of the rhombic nanowire is a result of the free surface induced heterogeneous nucleation of partial dislocations. Figure 3.5 provides a detailed account of the partial dislocation nucleation and the subsequent twinning process. The first partial dislocation nucleates at a large-angle vertex of the rhombic cross section as apparent in Figure 3.5a. The partial traverses the cross-section of the nanowire along a {111} slip plane and in doing so creates an intrinsic stacking fault in

the FCC lattice (Figure 3.5a-d). The deformation continues through defect-assisted deformation twinning where the stacking fault serves as a twin nucleus. In the deformation twinning process, partial dislocations nucleate at the low-angle vertex of the rhombic cross-section on adjacent {111} planes of the stacking fault at opposite ends, and propagate in a <112> direction, following the classical {111}<112> twinning system of the FCC lattice (Figure 3.5e-h). When the partials have swept the {111} plane and reached the free surface, this process is repeated. The motion of the partial dislocations serves to advance the coherent twin boundaries along the nanowire length, and in the process, restores the FCC stacking sequence through the aforementioned lattice reorientation.

3.3.2 *Top-Down* Truncated-Rhombic Silver Nanowires

The experimentally observed truncated-rhombic geometry demonstrates promising mechanical integrity for nanometer scale devices due to the small difference between the yield stress and the stress sustained during plastic flow. The nanowire retains nearly 75% of its strength for over half of the total strain-to-failure. The stress-strain response is presented in Figure 3.3b, while the snapshots of deformation are shown in Figure 3.6. As in the case of the rhombic nanowire, plastic deformation is facilitated by the nucleation of partial dislocations leading to the formation of a stacking fault. However, the truncated-rhombic nanowire does not undergo deformation twinning; instead, the deformation is constrained to the motion of more isolated partial dislocations. The dislocations move in a 'stair-rod' fashion, leaving behind a network of stacking faults in the nanowire, similar to the deformation substructure observed in the reoriented rhombic nanowire at much larger strain (Figure 3.4d). The stair-rod structure is first

observed in the middle region of the nanowire (Figure 3.6b), and with increasing strain the network expands along the entire length of the nanowire (Figure 3.6c). The limited cross sectional area of the nanowire combined with the stair-rod stacking fault structure confines the subsequent nucleation and motion of additional dislocations to a localized region. As a result, the nanowire begins to dissipate the accumulated strain energy through necking as displayed in Figure 3.6d.

The mechanism responsible for incipient plasticity in the truncated-rhombic nanowires is the nucleation and motion of Shockley partial dislocations. The first partial dislocations are heterogeneously nucleated at the intersection of a {100} and {111} free surface of the nanowire and create a stacking fault as they move through the cross-section (Figure 3.7a-c). Next, partial dislocations are nucleated at the intersection of the initial stacking fault and the {100} surface (Figure 3.7d), forming additional stacking faults in the previously mentioned stair-rod structure. The deformation then takes a path different than the rhombic nanowire. Deformation twinning begins via the nucleation and propagation of partial dislocations adjacent to the initial stacking fault, but is prevented as the partial dislocations are blocked by the stacking fault formed previously as part of the stair-rod structure (Figure 3.7e,f). These partial dislocations recede (Figure 3.7g), leaving a dislocation free stacking fault structure along the length of the nanowire (Figure 3.7h). Consequently, the truncated-rhombic nanowires show limited plastic flow and fracture at a much lower strain than the rhombic wires, which experienced very large strain enabled by deformation twinning.

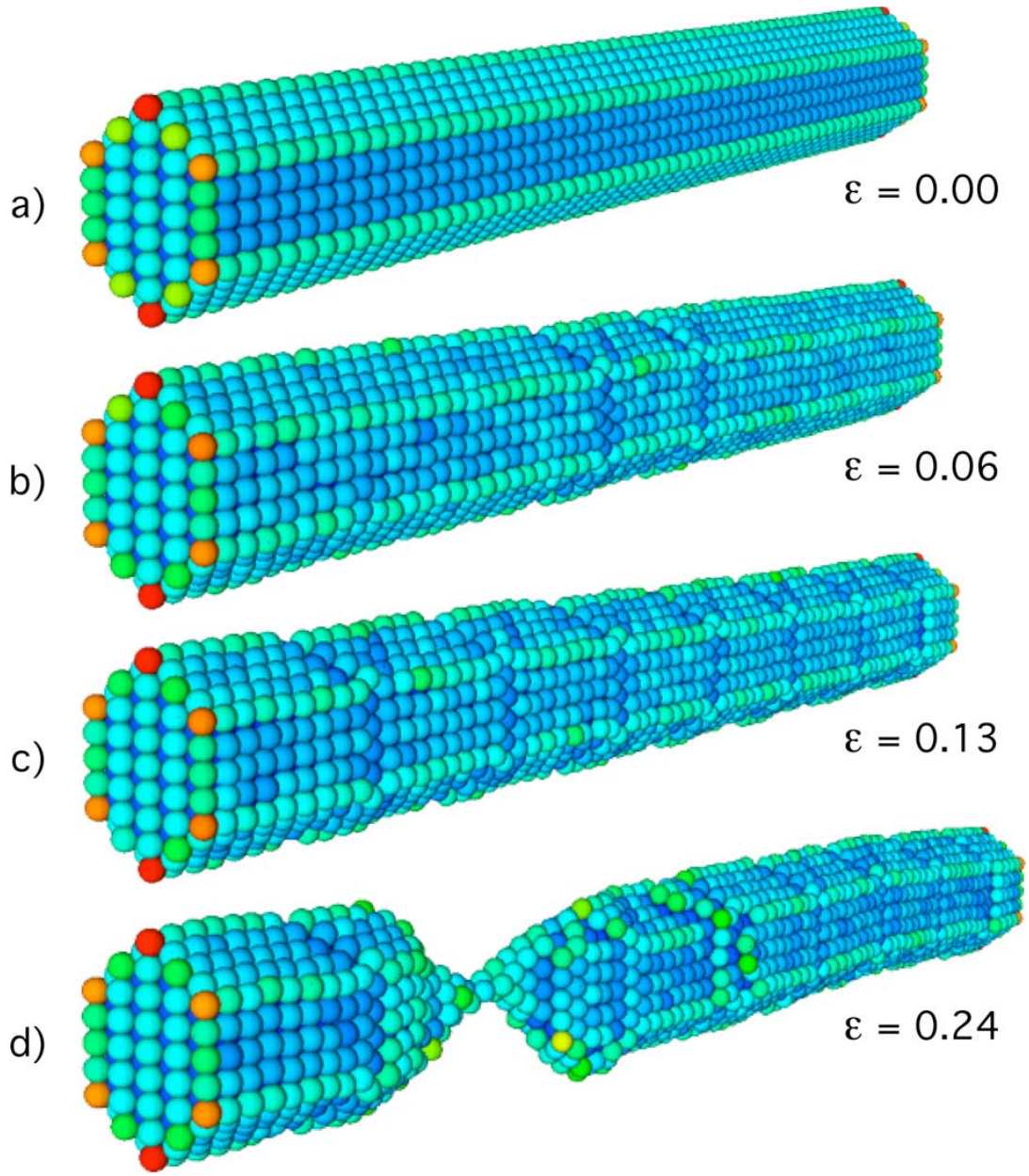

Figure 3.6: Snapshots of a truncated-rhombic silver nanowire during tensile deformation at 300 K. The strain value for each snapshot is indicated and corresponds to the stress-strain response in Figure 3.3b.

3.3.3 *Bottom-Up* Pentagonal Silver Nanowires

The pentagonal nanowires possess the lowest cohesive energy of the three structures considered. The pentagonal structure is stabilized by internal twin boundaries

that span the length of the nanowire. In addition to energetic stability, these twin boundaries provide an internal barrier to dislocation motion, which classically should result in high strength and low ductility. From the tensile response in Figure 3.3c, high strength is indeed observed. The pentagonal nanowires may be considered a multi-shell structure, consisting of concentrically stacked pentagonal shells. In this sense, the tensile deformation of the pentagonal wires may be easily described: deformation is initiated by fracture of the outer pentagonal shell at the intersection of two {100} free surfaces. The fracture event is accompanied by a large decrease in axial stress; this results from the dissipation of accumulated elastic strain energy through the severing of electron-dense, nearest-neighbor metallic bonds. The outer shell fracture and the resulting deformation are illustrated in Figure 3.8. As apparent in Figure 3.8b, the outer pentagonal shell fractures at several locations around the perimeter of the nanowire. Further deformation is achieved through the motion of dislocations within the vicinity of these fracture sites. Since the deformation is restricted to a small volume, the nanowire quickly begins to neck (Figure 3.8c), and with further applied strain a stable two atomic-strand nanobridge is formed before final failure. Stable nanobridges longer than two atoms are not experimentally observed during the extension of <110> oriented *top-down* nanowires [79], which is consistent with the predictions herein; however, interestingly, we predict their occurrence for the extension of <110> pentagonal nanowires.

The limited motion of partial dislocations within each wedge-shaped crystal of the nanowire characterizes the early deformation in the pentagonal nanowire. From the initial fracture location, Shockley partial dislocations are emitted and traverse a {111} plane in a <112> direction until reaching an internal twin boundary, leaving behind a

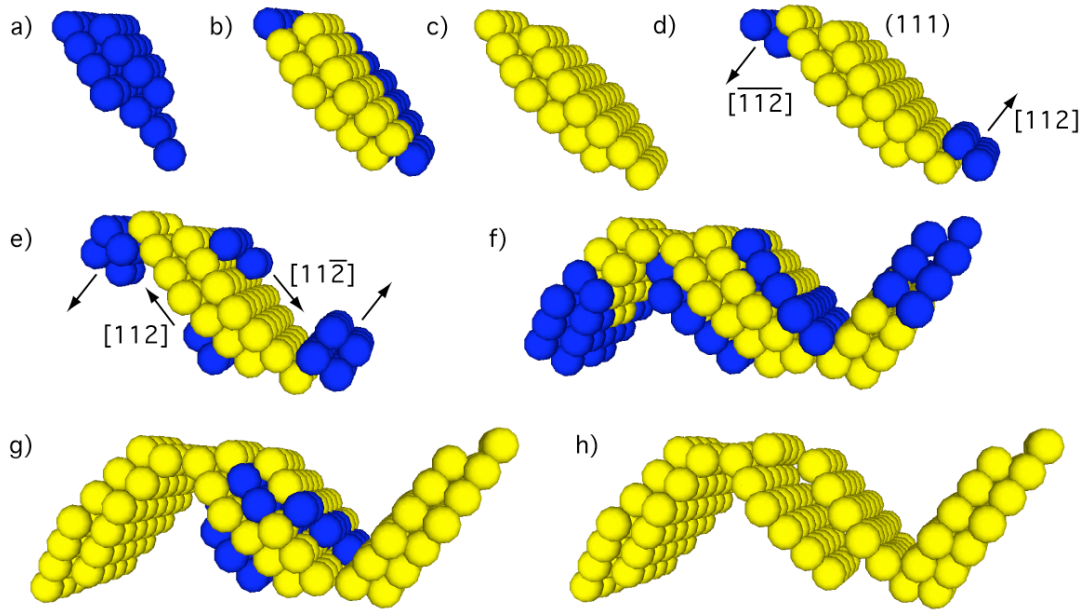

Figure 3.7: Stacking fault formation (a-c) and partial dislocation propagation (d-h) in a truncated-rhombic silver nanowire subjected to tensile deformation at 10 K. The atoms are colored as in Figure 3.5.

stacking fault in the process (Figure 3.9a-c). After reaching the twin boundary, the partial dislocation becomes immobilized thus causing an accumulation of energy which is then released through fracture at a new location on the outer shell (Figure 8d). This process continues until each wedge-shaped crystal is saturated with stacking faults, signifying complete circumferential fracture (Figure 8e-g). Complete circumferential fracture occurs at two locations along the nanowire length, separated by a finite distance. These circumferential fracture sites then bound the region in which further deformation occurs.

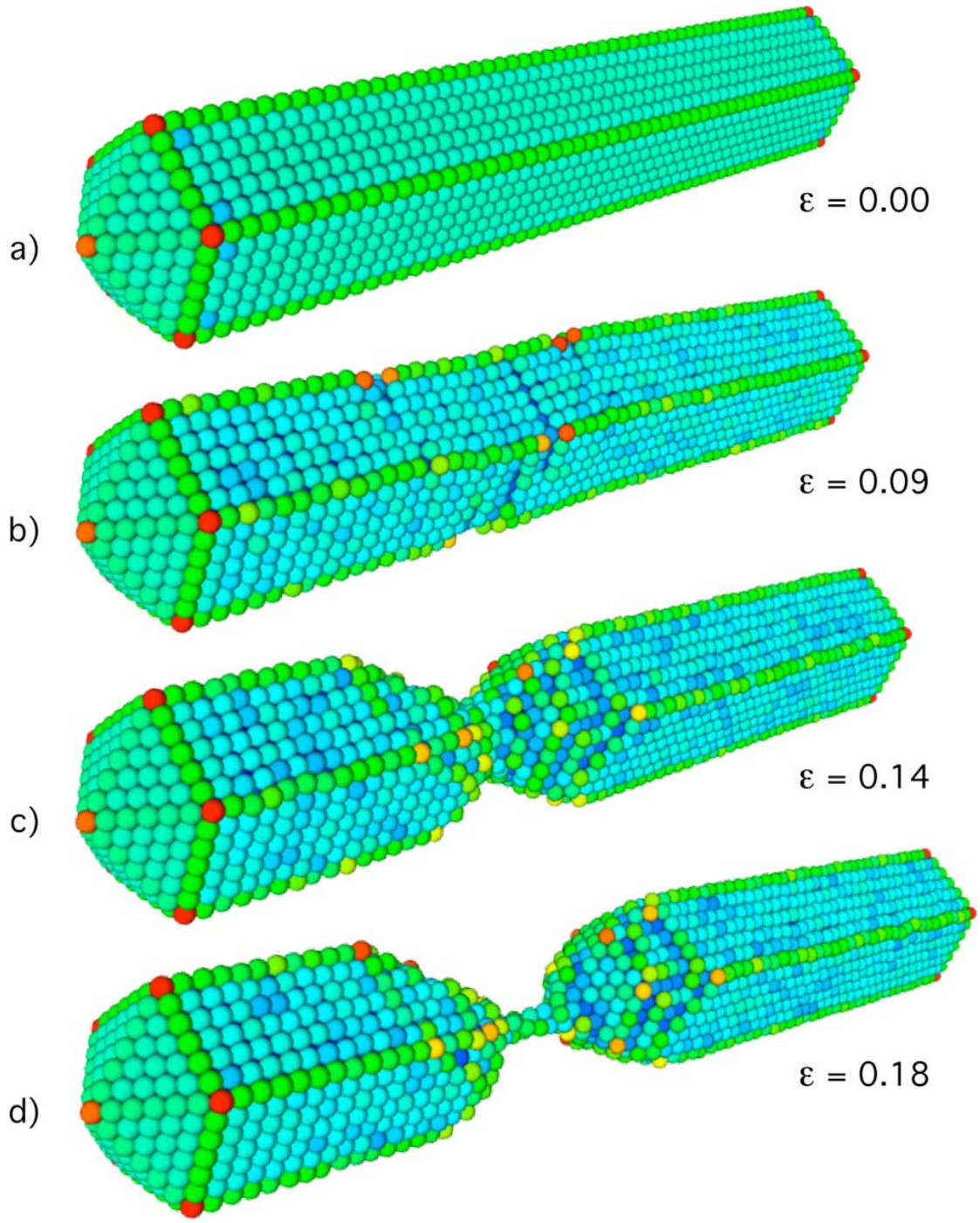

Figure 3.8: Snapshots of a pentagonal silver nanowire during tensile deformation at 300 K. The strain value for each snapshot is indicated and corresponds to the stress-strain response in Figure 3.3c.

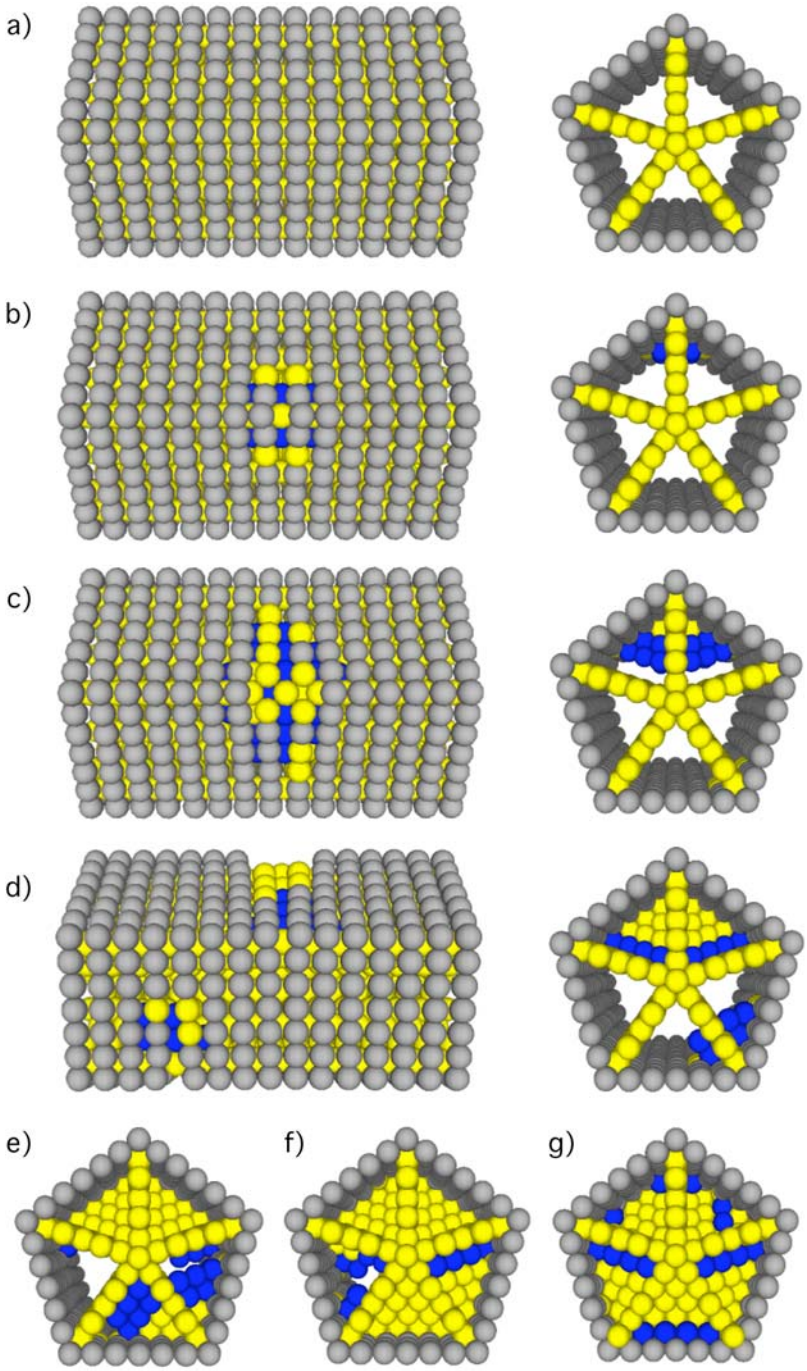

Figure 3.9: Outer shell fracture of a pentagonal silver nanowire (a-d) and corresponding partial dislocation nucleation (a-g) during tensile deformation at 10 K. A side view and a cross sectional view is shown for (a-d). Note that the wire is rotated in (d), showing fracture on the upper and lower surface of the wire. Complete circumferential fracture is evidenced through the defect structure in (e-f). The atoms are colored as in Figure 3.5; in addition, atoms with a surface coordination are shown in grey. The internal twin boundaries are colored yellow, as they have the same centrosymmetry as a stacking fault.

3.3.4 Size effect on yield strength

The tensile yield strength of the three nanowires is revealed to be strongly size and geometry dependent. For all three nanowire geometries, we observe decreasing yield strength with increasing nanowire diameter, as shown in Figure 3.10. The pentagonal nanowires provide the highest strength for all diameters considered, followed by the rhombic and truncated-rhombic geometries, respectively. Although, the magnitude of the yield strength is sensitive to the strain rate and also to the volume parameter used in the calculation of the virial stress, the relative strength of the three will not be affected by a change in these parameters. The size effect will be further discussed in the following section.

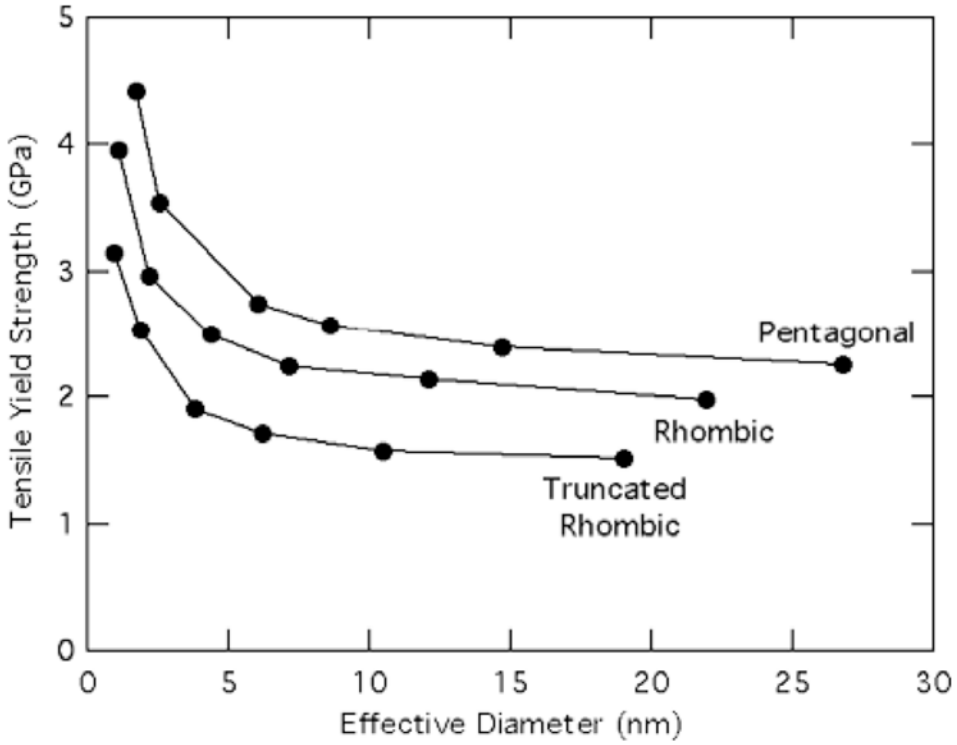

Figure 3.10: Size effect on the tensile yield strength of pentagonal, rhombic, and truncated-rhombic silver nanowires.

3.4 Discussion

Our results indicate that the mechanical behavior of energetically stable nanowires is strongly dependent on the cross-sectional geometry and surface orientation. Since the geometry and internal stability are directly linked to fabrication, we infer that the method of fabrication (*top-down vs. bottom-up*) has a dominant influence on mechanical strength and the mechanisms of deformation.

3.4.1 *Top-Down* Deformation Behavior

The total cohesive energy of a nanowire can be approximated as the summation of the contribution from atoms at free surfaces and the interior (non-surface) atoms. The local minimum energy configuration for an atom in an FCC lattice is to be surrounded by 12 nearest neighbors, each at an equivalent distance away. Surface energy is the consequence of this condition not being fully satisfied. The number of nearest neighbors is dependent on the atomic density of the surface being considered. For this reason, the magnitude of the surface energy is dependent on the surface orientation: for FCC materials, the close packed {111} surfaces have the lowest surface energy, followed by {100} and then {110} type surfaces. In bulk materials, surfaces comprise a minimal portion of the total volume, and thus the surface energy contribution is minimal. In nanowires, free surfaces constitute a considerable portion of the total volume, and the effect of surface energy is no longer insignificant. Atoms at free surfaces will minimize their energy by contracting towards the interior of the nanowire to maximize their local atomic density. As a result, tensile surface stresses induce an intrinsic compressive stress in the nanowire interior. The extent to which this surface stress induced compressive stress influences nanowire stability depends on the axial orientation. For elastically soft

axial orientations, (e.g. <100>), the surface stress is capable of inducing structural transformations [65, 66], while for the stiffer <110> orientation, the influence of surface stress is less significant.

It has been previously noted that free surface orientation influences the operant deformation modes in metallic nanowires [39] however, whether the influence is of an energetic or crystallographic origin is not fully understood. Since the truncated-rhombic nanowires differ from the rhombic ones only by free surface orientation, we perform a systematic comparison of the deformation observed in the two geometries in order to clarify the effect of surface orientation on mechanical behavior. The initial defect nucleation in both the rhombic and the truncated-rhombic nanowires results in the formation of a intrinsic stacking fault. After the formation of the first stacking fault, the deformation paths of the two-nanowire geometries deviate from a common path.

As presented previously, silver nanowires with a rhombic cross-section completely bounded by {111} surfaces mechanically deform through deformation twinning. A defining characteristic of this type of deformation is the shape change produced during deformation. The shape change is restricted by the crystallography of the cross-section. For the rhombic nanowire, the shape change is evidenced through the conversion of the cross-section geometry from rhombic to rectangular during the {111}<110> to {100}<100> lattice reorientation. The {111} free surface and <110> axial orientation of the rhombic nanowires creates an ideal crystallographic path for the shape change to occur thus allowing deformation twinning to control the mechanical response.

The truncated-rhombic nanowires were predicted to deform by the organized motion of partial dislocations, which form a 'stair-rod' structure along the nanowire length. The {100} surfaces exposed from the truncation of the rhombic cross-section prevent the shape change that must be accommodated for deformation twinning to occur. We conducted simulations with varying levels of truncation to elucidate this effect. Interestingly, our results indicate that the likelihood of twinning as a mechanism of deformation is determined by the extent of truncation. Nanowires with a less severe truncation than those presented in Section 3.2 were observed to deform via competing mechanisms of twinning and slip. As the extent of truncation is reduced from that in Section 3.2 the propensity for twinning is increased. For the nanowires with a reduced truncation, the deformation twinning results in the transformation of {111} surfaces to {100} as in the case for the perfect rhombic wires, and interestingly, the {100} surfaces of the truncated faces are reoriented to {110}, thus following the hierarchical order of surface energies for the FCC lattice ($E_{\{111\}} < E_{\{100\}} < E_{\{110\}}$).

The implication of these results is that the influence of surface orientation on twinning as a mode of deformation is primarily crystallographic. In order for twinning to be the operant mode of deformation, there must exist a minimum energy path to accommodate the shape change produced from the lattice reorientation. Clearly, truncating the rhombic nanowire alters the energetic landscape for deformation. While we cannot conclude the exact nature of the energetic barrier to deformation twinning in the truncated-rhombic nanowires, we can conclude the following: with increasing truncation of the rhombic nanowire, it becomes more favorable to activate slip on a

secondary system than to propagate the coherent interfaces of the initial stacking fault on the primary slip system. This topic is the focus of the research presented in Chapter V.

3.4.2 Bottom-Up Deformation Behavior

The prevailing structural feature of *bottom-up* nanowires is internal stability. Contrary to *top-down* nanowires, *bottom-up* structures maintain a stable atomic configuration during the fabrication process. Mechanically, this internal stability creates two effects: it provides a larger energetic barrier to defect formation and in the special case of the multiply twinned pentagonal nanowire, it limits ductility by hindering the motion of defects. The ensuing mechanical behavior is expected; the nanowires exhibit high strength and localized plastic deformation with a relatively low strain to failure.

The internal stability of the pentagonal nanowire arises from the five coherent twin boundaries that span the nanowire length. Similar to the *top-down* nanowires, the initial defect in the pentagonal nanowire is heterogeneously nucleated at the intersection of two external surfaces. In fact, the nucleation site may be considered as the intersection of the internal, coherent twin boundary with the free surface. In the *top-down* wires, the nucleated partial dislocations glide along the slip planes, undisturbed by internal planar defects. For a single crystal nanowire, the relation between the axial orientation and the loading direction determines the crystallographic slip systems that may be activated when a critical resolved shear stress is overcome: this is the basis of a Schmid factor analysis. Typically, this approach does not apply to polycrystalline materials; however, since each crystal in the pentagonal nanowire possesses a common <110> texture and span the length of the wire, the approach is acceptable. However, the pentagonal nanowires

present a more complicated scenario, since the nucleation site is bisected by an internal twin boundary.

The distinguishing characteristic of the initial deformation in the pentagonal nanowires is the fracture of the outer pentagonal shell. We find that fracture as a mechanism of deformation is justified for two reasons. First, the internal twin boundary prevents the unimpeded dislocation motion is observed in the initial nucleation event in the *top-down* nanowires. Secondly, the twin boundary is aligned with the tensile axis, thus the boundary is experiencing the maximum possible tensile stress from the imposed loading conditions. Given that the stress state is maximized on the twin boundary, and the dislocation nucleation is impeded by the same twin boundary, the consequence is atomic separation (fracture), along the twin boundary. The limited ductility observed in the pentagonal wires results from the motion of the partial dislocations that are emitted during the fracture event. The motion of these partials is restricted by the internal twin boundaries, an additional strengthening mechanism arising from the internal stability.

3.4.3 Size Effect on Yield Strength

The magnitude of the yield strength of nanowires is controlled by two factors. First, the elastic modulus (stiffness) determines the rate of change of the tensile stress with strain in the nanowire and secondly, for a specific geometric configuration, a critical activation energy must be attained before a defect is nucleated in the nanowire. With respect to the first, if the yield strain is held constant, the yield strength will scale directly with the elastic modulus: a high stiffness will result in a higher yield strength than will a low stiffness, for an equivalent yield strain. The nucleation site in the nanowire determines at what strength the activation energy will be attained, and a defect will

nucleate. For all three nanowires, we observe the nucleation at a corner formed at the intersection of two free surfaces. In essence, the corners act to locally magnify the stress state, thus controlling the stress required to attain the activation energy for defect nucleation. Accordingly, a variation in the elastic modulus or nucleation site will affect the magnitude of the yield strength.

To determine the dominant contribution to the yield strength size effect, we determined the elastic modulus for all nanowires from molecular statics calculations. The rhombic and truncated-rhombic nanowires show a nearly identical elastic modulus as a function of nanowire diameter, while the pentagonal nanowires are considerably stiffer over the same range of diameters. It is apparent, from Figure 3.10, that the pentagonal nanowires show the highest yield stress followed by the rhombic, then the truncated-rhombic nanowires. We conclude that the pentagonal nanowires exhibit higher yield strength primarily from the increased elastic modulus relative to the other nanowire geometries. Also, defect nucleation at a free surface corner in the pentagonal nanowires is inhibited by the internal twin boundaries. This raises the activation energy, and thus the strength required for defect nucleation increases. The difference between the yield strength of the rhombic and the truncated-rhombic is more concise. Since the rhombic and truncated-rhombic geometries have the same elastic modulus size dependence, the yield strength difference must be related to the nucleation event. Indeed, as discussed earlier, the nucleation site for the two nanowires is different. The nucleation site in the truncated-rhombic nanowires imparts a larger stress amplification than does the nucleation site in the rhombic nanowires, this results in a lower stress required to reach the activation energy for defect nucleation.

3.5 Conclusion

The deformation behavior of experimentally observed <110> oriented silver nanowire structures was determined using atomistic simulations. *Top-down* nanowires with rhombic and truncated-rhombic cross-sections and *bottom-up* nanowires with a multiply twinned, pentagonal structure were analyzed. The mechanical response from zero strain to failure was presented for each nanowire, and the mechanisms of deformation were discussed in detail.

The operant deformation mechanism was revealed to depend strongly on the structure of the nanowire. Rhombic nanowires with {111} side surfaces were observed to deform by deformation twinning, and consequently deformed to over 40% strain before failure. The truncated-rhombic nanowires which possess {100} in addition to the {111} surfaces, deformed by forming a 'stair-rod' structure of stacking faults along the nanowire length, arising from the widespread motion of partial dislocations. The multi-shell pentagonal nanowires yielded by fracture of the outermost pentagonal shell.

We also presented a structure-dependent size effect on the tensile yield strength of the nanowires. The strength was observed to be inversely proportional to the nanowire diameter and to be strongly dependent on the geometry of the nanowire. The pentagonal structure demonstrated the highest strength of the three structures, which we credit to the enhanced stiffness and internal resistance to deformation provided by the internal twin boundaries of the nanowire. The difference in strength between the rhombic and truncated-rhombic nanowires is attributed to the variation in free surface configuration, which alters the initial defect nucleation event.

The overarching premise of this work is that metallic nanowires may be tailored to the mechanical requirements of a functional device based on structure.

CHAPTER IV

ELASTIC BENDING BEHAVIOR OF METAL NANOWIRES

4.1 Introduction

The mechanical behavior of nanometer scale structural elements has been increasingly examined in recent years. In particular, the mechanical properties and structure of nanowires have undergone much investigation. In general, mechanical behavior on the nanometer scale differs from that of bulk materials primarily due to the influence of free surfaces. Atoms at or near a free surface experience reduced coordination due to a different local binding environment than in the interior of a lattice. As a consequence of under-coordination, surface atoms exhibit a higher energy (*surface energy*) than atoms in the bulk of a material. In bulk materials, surfaces make up a minimal fraction of the total volume; therefore, the effects of surface energy are insignificant. However, in materials with nanometer scale dimensions, surface atoms comprise a significant fraction of the total volume of the material, and surface energy effects are no longer negligible. In nanowires, surface atoms will contract towards the core of the nanowire to minimize their energy by maximizing their local electron density. This surface contraction results in tensile surface stresses and intrinsic compressive stresses in the nanowire core, which have been predicted to significantly impact the mechanical properties and structure of nanomaterials [91, 93, 97]. Both atomistic simulations

and experiments have been undertaken to probe the mechanical behavior of nanowires and to reveal the effects that free surfaces play in nanowire behavior.

At the bulk scale, mechanical properties are typically obtained through tests that apply a uniaxial tensile load to a specimen of a specific geometry. However, few experiments have mechanically tested nanowires or nanotubes under uniaxial tension due to difficulties in physically applying and measuring tension deformation on such a small scale (a study by Yu *et al* [98] is a notable exception involving carbon nanotubes). Despite these difficulties, experimental techniques for determining the elastic properties and plastic deformation characteristics of nanowires and nanotubes have been developed which apply a transverse load rather than an axial one. One method involves measuring elastic properties, including Young's modulus, by inducing electromechanical resonance in individual nanowires or nanotubes inside a transmission electron microscope or atomic force microscope (AFM) [85, 86, 99, 100]. Nanoindentation of metallic and semiconductor nanowires has also been used to determine elastic properties [101, 102]. Recently, a method has been developed which utilizes an AFM in contact mode to apply a bending force to a single nanowire or nanotube in a single- or double-clamped configuration [87, 88, 103-112]. The force-deflection response obtained from the AFM experiments is then analyzed with continuum elastic bending theory to extract the elastic modulus of the nanowires [104]. Specific results obtained by Wu *et al* [88, 103] for silver and gold nanowires show that the Young's modulus is comparable to the bulk modulus and that it is essentially independent of nanowire diameter, while in other AFM bending investigations, the Young's modulus of silver nanowires was found to increase with decreasing diameter [87].

Inherent complexities and unknowns associated with controlling experimental test conditions on the nanometer scale have led to the extensive use of atomistic simulation as a complementary method to examine the mechanical properties of nanowires. Specifically, molecular dynamics (MD) simulations using the embedded atom method (EAM) have been employed to examine the mechanical response and energetics of face-centered-cubic (FCC) metal nanowires [34, 39, 52, 65, 67, 69-71, 73, 74, 94, 113-115]. For instance, a study by Diao *et al* [67] on nanowire elasticity showed that the elastic modulus depends on size. Furthering this idea, Liang *et al* [94] demonstrated that the Young's modulus of single-crystal copper nanowires increases or decreases with decreasing size, depending on the axial orientation of the nanowire. Size effects have also been shown to exist in regard to the tensile strength of nanowires; smaller wires have been predicted to exhibit higher strengths [34, 113].

The majority of previous computational studies have focused on the mechanical analysis of metal nanowires subjected to uniaxial tension, due to the ease of analysis of the tensile stress state. Although computational studies of the bending behavior of nanowires have been pursued, these investigations have primarily focused on dynamic deformation mechanisms instead of elastic properties [116, 117] In a work by Wu [118], the bending response of a copper nanowire is found to differ from continuum calculations. A study by Miller and Shenoy [92] relates nanowire tensile and bending behavior and predicts that the nanometer scale size effect on the elastic properties of nanowires is dependent on the applied stress state; namely, pure bending and uniaxial tension. It was reported that surface stress should have an amplified effect on the elastic properties of a nanowire subjected to bending than a nanowire under a tensile load since under bending,

the induced axial stress is highest at the free surfaces, while the induced axial stress for a specimen under tension is essentially uniform through the cross-section. While these works have proven important, a comprehensive understanding of the differences in the elastic behavior of nanowires under bending and tensile stress states has yet to be presented.

The disparity in common experimental and computational testing methods raises concerns related to the measurement of elastic properties in nanowires. For instance, to what extent does surface energy and surface stress affect the elastic properties of metal nanowires determined by bending deformation, and how do the elastic properties measured in bending compare to those established for tensile deformation? Also, most experimental and computational studies have utilized continuum-mechanical frameworks to analyze the mechanical behavior of nanometer scale elements. It is unclear whether such analyses yield different results for tensile and bending stress states due to variations unseen in bulk materials. The objective of the present study is to use EAM molecular statics calculations to investigate the bending and tensile behavior of silver nanowires of varying axial and surface orientation to systematically determine the impact of nanowire structure, geometry, and applied stress state on the resulting elastic response.

4.2 Methodology

Four different nanowire structures were considered for the analysis; the cross-sectional geometries and crystallographic characteristics are presented in Figure 4.1.

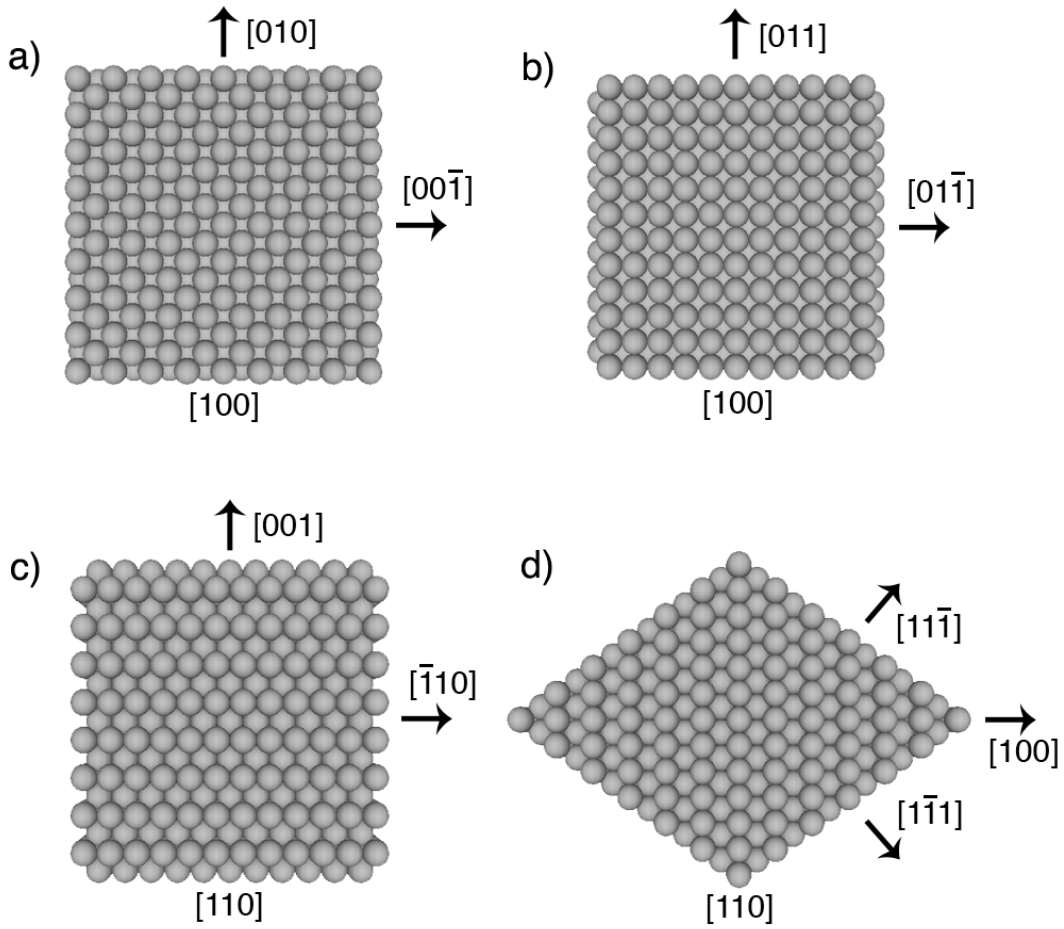

Figure 4.1: Cross-sectional geometries of the four silver nanowires under consideration. (a) and (b) are axially oriented in the [100] direction while (c) and (d) are axially oriented in the [110] direction. (a) and (b) have square cross sections and are bound by {100} and {110} surfaces, respectively. (c) has a rectangular cross section that is bound by both {110} and {100} type surfaces. Finally, (d) has a rhombic cross section and is faceted by low-energy {111} surfaces.

These nanowires were chosen to provide a wide array of different structures and surface orientations for analysis. All nanowires were created with a length-to-thickness ratio of eight, where thickness is defined as the vertical cross-sectional distance in Figure 4.1.

4.2.1 Computational Techniques

For all simulations, the nanowires were created with atoms in positions corresponding to a bulk FCC crystal lattice. Periodic boundary conditions were not imposed in any direction. Before either the bending or tension loading processes occurred, the nanowires underwent energy minimization using the conjugate gradient method; this energy minimization causes atoms near free surfaces to contract. After the initial relaxation, the nanowires subjected to bending deformation were loaded according to the following incremental displacement-relaxation method, which is illustrated in Figure 4.2.

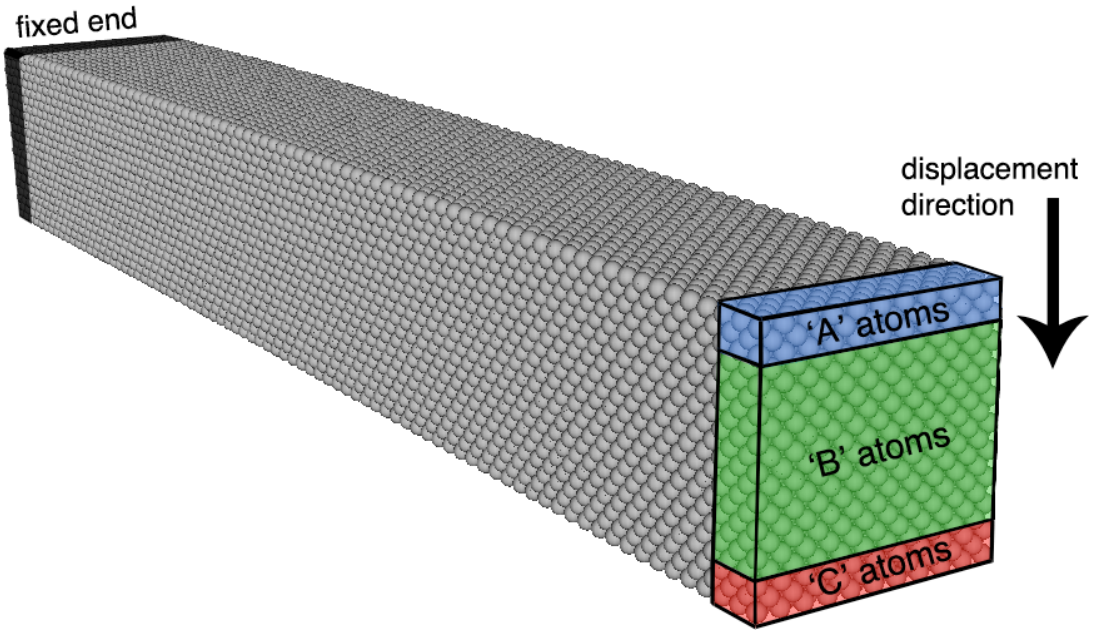

Figure 4.2: Schematic showing the bending process.

Atoms at one end of the nanowire were constrained with a zero force boundary condition (the "fixed end" in Figure 4.2); these atoms remained fixed in their positions

during the entire incremental loading process. At the other end, atom types ‘A’, ‘B’, and ‘C’ were displaced vertically downward 0.1 nm. A section of atoms at the top edge of this displaced end (‘A’ atoms) was then held fixed with zero force while the rest of the nanowire was allowed to relax to a state of minimum energy. Next, a section of atoms at the bottom edge of the displaced end (“C” atoms) was held fixed with zero force while the nanowire again underwent energy minimization. After the second relaxation, the entire displacement-relaxation cycle was repeated for a desired number of increments. The total equilibrium minimum energy and the deflection profile of the nanowire were recorded after the second relaxation of each increment. The double relaxation during each increment is necessary because it allows the wire to conform to a natural deflection profile and it removes any artificial axial tension induced during the displacement process. Fixing only the top (type ‘A’ atoms) or bottom (type ‘C’ atoms) sections of the displaced end during each energy minimization routine allows the portions of the displaced end that are not fixed to rotate slightly to fit with the rest of the nanowire. Simulations with only one relaxation per increment were initially attempted, but they resulted in inconsistent modulus values and unrealistic deflection profiles.

The incremental tensile loading process involved similar procedures. After the initial energy minimization, atoms at one end of the nanowire were fixed, and a linearly varying displacement profile was imposed along the axial direction of the remainder of the nanowire. The displacement profile varied from zero at the fixed end to 0.2% strain at the opposite end, per loading increment. Atoms at the displaced end were then fixed and the nanowire was relaxed in order to obtain the potential energy of the strained nanowire. This incremental process was repeated until 2.0% strain was reached.

4.2.2 Calculation of the Elastic Modulus

The effective Young's modulus of the nanowires from the bending simulations was calculated by using a method derived from continuum beam theory. For small deflections caused by a concentrated load, the strain energy ΔU in a cantilever beam is given by

$$\Delta U = \int_0^L \frac{EI}{2}\left(\frac{d^2\nu}{dx^2}\right)^2 dx \tag{4.1}$$

where L is the length, E is the Young's modulus, I is the moment of inertia, ν is the beam deflection, and x is the coordinate along the axial direction.[119] The nanowires under consideration can be represented by a cantilever beam in which a bending moment and shear forces are present. In (4.1), only the effects of the bending moment on the strain energy are considered; since, if a cantilever beam is sufficiently long ($L/t > 8$, where t is thickness), then the energy due to shear deformation may be neglected [119]. A length to thickness ratio of eight was used for all nanowire simulations in this study. From continuum theory, the deflection ν of a cantilever beam with a concentrated load P at one end is given by

$$\nu = -\frac{Px^2}{6EI}(3L - x) = -\frac{\delta_B x^2}{2L^3}(3L - x) \tag{4.2}$$

where δ_B is the maximum deflection at the free end of the beam [119]. The second derivative of (4.2) is

$$\frac{d^2v}{dx^2} = \alpha - \beta x \tag{4.3}$$

in which $\alpha = 3\delta_B/L^2$ and $\beta = 3\delta_B/L^3$. At each displacement increment, the deflection along the length of the nanowire is fit to the theoretical model in (4.2), and the two constants α and β are calculated from the best-fit curve. Figure 4.3 shows the actual deflection curve and the best-fit theoretical model given by (4.2) from a nanowire bending simulation.

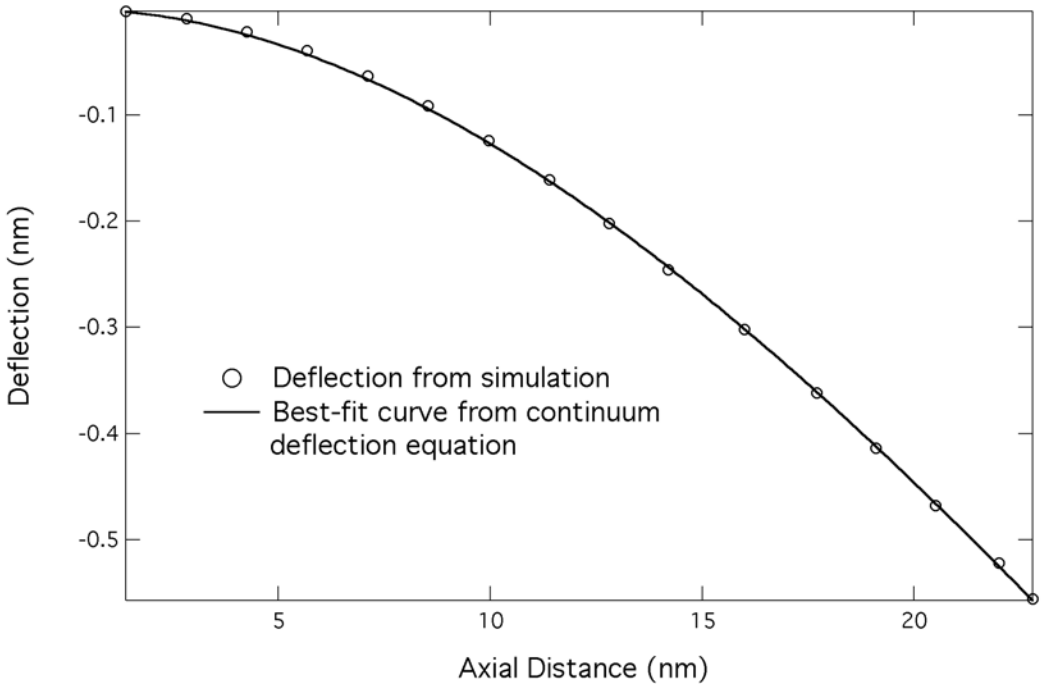

Figure 4.3: Theoretical and actual deflection profiles for a <110> axially oriented rectangular nanowire bent perpendicular to a (100) lateral plane. This figure shows the deflection at the sixth bending increment.

After fitting the deflection curve to the theoretical model and determining the constants α and β, the Young's modulus E for each nanowire is calculated at each bending increment from (4.4):

$$E = \frac{2\Delta U}{I L\left(\alpha^2 - \alpha\beta L + \frac{1}{3}\beta^2 L^2\right)} \tag{4.4}$$

In (4.4) the Young's modulus is determined by inserting the second derivative of the theoretical deflection equation (4.3) into the strain energy expression (4.1) and integrating. This method gives an expression for Young's modulus that is only a function of strain energy, deflection, and geometric parameters; forces or stresses are not expressly used at any point in calculating the Young's modulus.

The moment of inertia (I) is calculated using continuum equations. For rectangular cross sections, $I = h^3 b/12$, where h and b are the height and width of the relaxed cross section, respectively [119]. It should be noted that for the <110> axially oriented square wires (Figure 4.1c), the width w is not clearly defined because alternating rows of atoms protrude from two side surfaces. By convention, the width w is defined to be bound by the average coordinate values of the outermost two layers of atoms on each side of the nanowire cross section. For rhombic cross sections, the moment of inertia I is given by

$$I = \int y^2 \, dA = 2\int_0^{\frac{1}{2}h} y^2 b\left(1 - \frac{2y}{h}\right) dy = b\left(\frac{1}{12}h^3 - \frac{1}{16}h^3\right) \tag{4.5}$$

where *b* is the length of the longer diagonal of the rhombic cross-section, *h* is the length of the shorter diagonal, and *y* is the coordinate parallel to the bending direction. Also, the strain energy ΔU for the nanowires is defined as the energy difference between the bent configuration and the initial state of minimum energy (obtained after the first relaxation). Since *E*-values were calculated for each bending increment, the reported values were taken to be the numerical average of the values from the third through sixth increments. However, the variation in *E*-values was usually no more than a few GPa.

A continuum-mechanical method for calculating Young's modulus for nanowires in tension was presented in a study by Diao *et al* [67]. At each tensile loading increment, the axial stress in the interior of the nanowire is balanced by the externally applied quasi-static force at the end of the nanowire. Thus, the change in potential energy in the nanowire during loading is equal to the work done by the externally applied load

$$\Delta U = \int_0^{\Delta L} F\, d(\Delta L) = \int_0^{\varepsilon} S\sigma L\, d\varepsilon = \int_0^{\varepsilon} V\sigma\, d\varepsilon \tag{4.6}$$

where *F* is the applied load, *S* is the area of the cross section perpendicular to the load, $\sigma = F/S$ is the average axial stress, $\varepsilon = dL/L$ is the axial strain, and *V* is the volume of the nanowire. Expansion of σ and *V* allows for the manipulation of (4.6) into the form

$$\frac{\Delta U}{V_0} = E\left[\frac{1}{2}\varepsilon^2 + \frac{1}{3}\zeta\varepsilon^3\right] \tag{4.7}$$

where E is the Young's modulus at $\varepsilon = 0$, V_0 is the initial volume, and ξ is a constant. Fitting the experimental strain energy versus applied strain data to (4.7) allows for calculation of E. More detailed information pertaining to this method can be obtained by consulting Diao *et al* [67].

4.3 Results and discussion

Figure 4.4 shows the calculated Young's modulus values for all of the tested nanowires as a function of size. It is evident from Figure 4.4 that for larger nanowires, the modulus values approach the bulk value; however, as nanowire thickness decreases, the Young's modulus deviates from the bulk value. The <110> axially oriented nanowires in 4a exhibit stiffening behavior as size decreases, while the <100> axially oriented nanowires in 4b exhibit softening behavior. Stiffening along the <110> direction and softening along the <100> direction with decreasing size have previously been observed in similar nanowire systems [94] and thin films [120]. From the data presented in Figure 4.4, it is apparent that the change in Young's modulus with decreasing size is more extreme for <110> axially oriented wires than for nanowires oriented in the <100> direction.

It is important to note that the modulus values from both bending and tension simulations show the same stiffening or softening trends for both nanowire geometries. However, the data also show a loading-method dependent size effect. For nanowires with the same geometry but different loading methods, the disparity in modulus values increases as wire size decreases. This is best illustrated in Figure 4.b, in which <100> axially oriented nanowires under bending loads soften at a greater rate than nanowires in tension as size decreases. In other words, the difference in modulus values is greater at

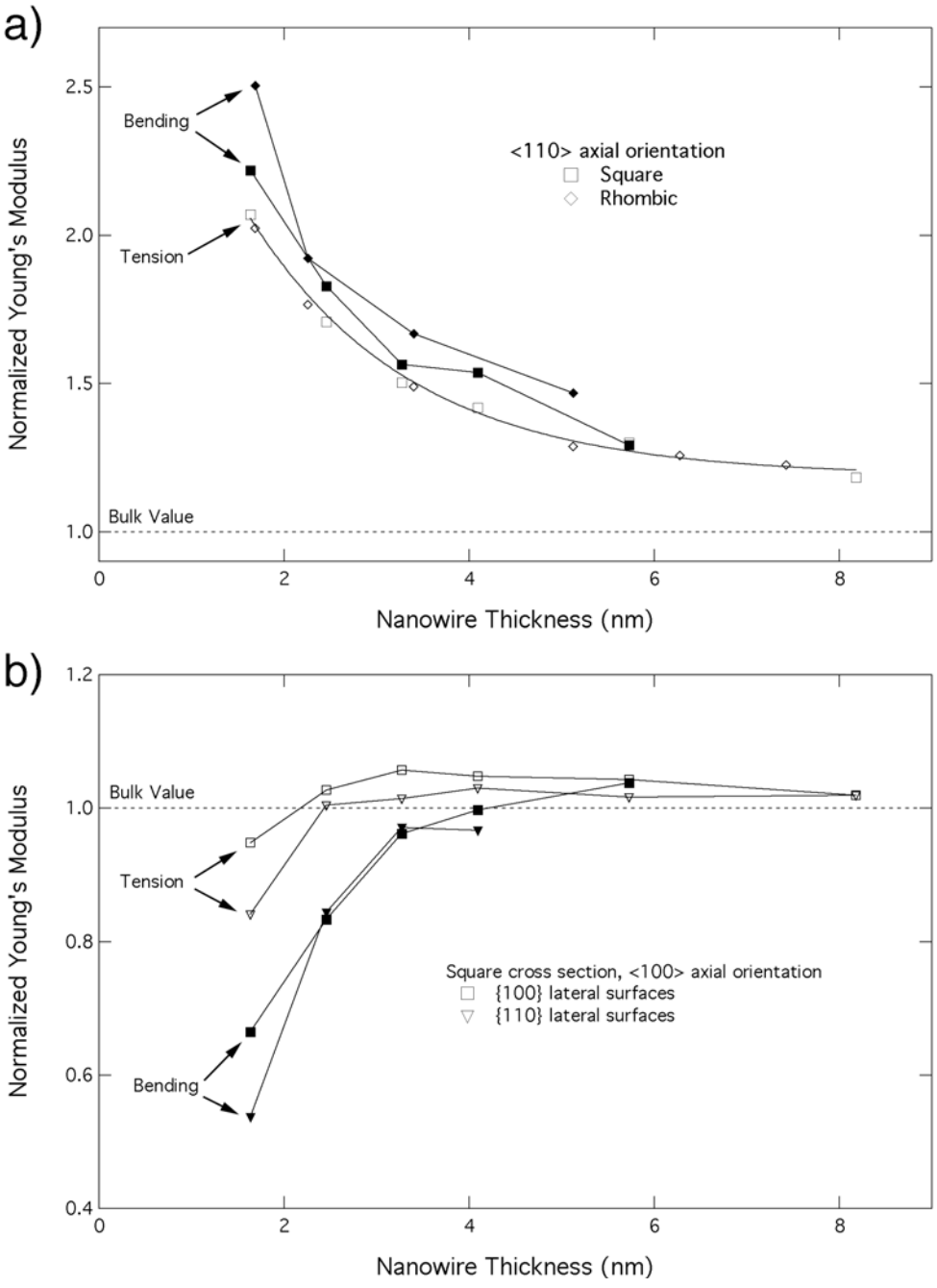

Figure 4.4: Young's modulus values obtained from bending and tension simulations for (a) <110> axially oriented nanowires with square and rhombic cross-sectional geometries, and (b) <100> axially oriented nanowires with square geometries. All values are normalized with respect to the bulk Young's modulus value for a <100> or <110> Ag single crystal (44.3 and 84.1 GPa, respectively). [121] The line fit to the tension data in (a) is intended to illustrate the trend in modulus values for rhombic and square nanowires in tension.

smaller sizes for the same nanowires in bending and tension. The trends in percent difference for the same <110> and <100> axially oriented nanowires in bending and tension are shown in Figure 4.5.

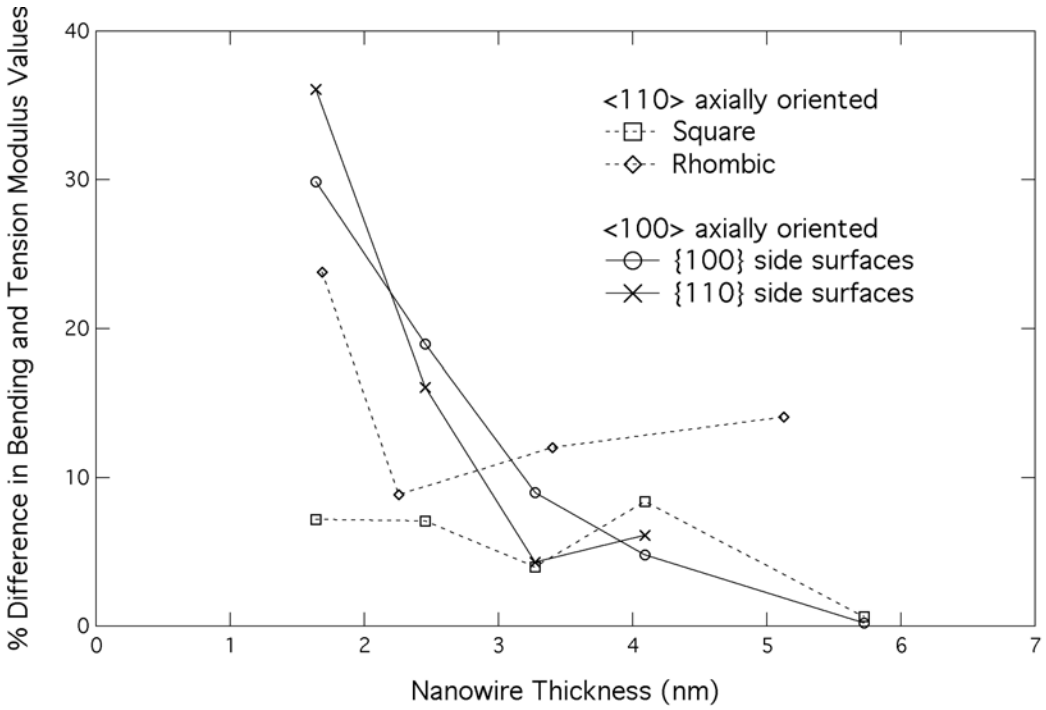

Figure 4.5: Percent difference in the modulus values for the same nanowires tested under different loads (bending and tension).

The percent difference parameter in Figure 4.5 is given by

$$X = \left| \frac{E_t - E_b}{E_t} \right| \tag{4.8}$$

where X is the absolute value of the percent difference and E_t and E_b are the modulus values from tension and bending simulations, respectively. Both geometries of the

<100> axially oriented nanowires clearly show an increase in percent difference between the two loading methods as size decreases. The <110> axially oriented nanowires show this loading method-dependent size effect to a lesser degree; the percent difference in modulus for the <110> wires increases to a lesser extent than for the <100> wires as size decreases. Specifically, the rhombic nanowires show a decrease in percent difference with decreasing size except for the smallest nanowire tested, which exhibits a much higher modulus value in bending than in tension. The percent difference for the modulus values from bending and tension simulations for <110> axially oriented square nanowires are all within 10%; these values show no discernible trend.

Another factor affecting the size-dependence of Young's modulus is the surface orientation. For <100> nanowires in Fig. 4b with different lateral surface orientations undergoing the same loading process, the smallest wires tested show the greatest difference in Young's modulus in both tension and bending. Rhombic and square <110> axially oriented nanowires (Figure 4.4a) show a modulus difference in bending, but in tension, there is no appreciable difference.

Overall, the Young's modulus size dependence may be separated into three regimes. For large sizes (t > 8 nm in Figure 4.4b), all nanowire modulus values approach the bulk single-crystal modulus value, regardless of loading method or free surface orientation. A transition region in which the modulus diverges from the bulk value begins to emerge as the size of the nanowires decreases to values just below the upper thickness bounds (4 < t < 8 nm in Figure 4.4b). In the final region, which contains the smallest nanowires (t < 4 nm in Figure 4.4b), the Young's modulus diverges for the same nanowires under different loading methods and for nanowires with the same axial

orientation but with different exposed surfaces. These three regimes are clearly defined over the size range of the nanowires in Figure 4.4b, but in Figure 4.4a, the boundaries of the regions are not as distinct. The <110> axially oriented nanowires in Figure 4.4b exhibit modulus size dependence over a broader size range than do the <100> axially oriented nanowires.

A few explanations for this seemingly anomalous elastic behavior have been postulated. Miller and Shenoy [92] predict that changes in elastic modulus in nanometer scale materials are due primarily to the influence of variable surface elasticity. Free surfaces in a material can have a different elastic modulus than the bulk due to changes in atomic coordination and electron distribution at the surface [120, 122]. As nanowire size decreases, the surface area-to-volume ratio increases; thus, the surface contribution to the overall modulus increases. This "core-shell" elasticity model has been widely accepted, but its efficacy in causing changes in the overall nanowire modulus has been disputed. Other factors have also been shown to cause the observed trends in modulus. A recent molecular dynamics study by Liang *et al* [94] demonstrates that the nonlinear elastic response of the nanowire core plays the greatest role in determining the elastic modulus of nanowires subjected to uniaxial tensile (or compressive) loads. This effect stems from the fact that in equilibrium, surface stresses give rise to axial compressive strain in the nanowire core. As nanowire size decreases, this compressive strain increases in magnitude because of larger surface area-to-volume ratios. Since single-crystal bulk metals exhibit a nonlinear elastic response when subjected to compressive stresses, the elastic modulus of the nanowire core changes with increasing compressive stress. Whether the elastic modulus increases or decreases is determined by the crystallographic

orientation of the lattice: the modulus decreases with increasing strain in the <100> direction, while it increases with increasing strain in the <110> direction [94].

The observed trends in elastic modulus shown in Figure 4.4 can be explained by integrating both of these ideas. More importantly, the use of two different loading methods in the simulations allows for the identification of which effect is dominant. For larger sizes, the nanowire modulus values approach the bulk values for both orientations; thus, free surfaces do not have an appreciable effect on the modulus for these wires. For both loading methods in Figure 4.4b, the elastic modulus decreases with decreasing nanowire size below a critical nanowire thickness. Regardless of loading method and the associated stress state, the nonlinear elastic effects on the modulus should result in modulus changes that are the same magnitude for each nanowire geometry. Since the bulk <100> direction has been observed to soften as a result of nonlinear elasticity [94], a certain amount of softening in the <100> axially oriented nanowires can be attributed to core nonlinear elasticity. However, the nonlinear elasticity model does not account for the greater degree of softening experienced by both nanowire geometries under bending loads rather than in tension. Presumably, this disparity is caused by the influence of surface elasticity. In nanowires under bending loads, the induced axial stress is concentrated at the upper and lower free surfaces. In nanowires subjected to uniaxial tension, the applied stress is uniform through the cross section. Since {100} and {110} surfaces have been shown to have lower values for the elastic modulus than in the bulk along the <100> direction [94, 120], it is expected that a nanowire bend test for the <100> axially oriented wires would yield lower modulus values than a tensile test due to the preferential sampling of the surface. Also, the increase in percent difference of modulus

values in bending and tension as wire size decreases can be explained by the heightened influence of surface elasticity in bending. Both of these features are observed in the modulus data for the <100> axially oriented nanowires in Figure 4.4b and Figure 4.5.

It is more difficult to distinguish the individual mechanisms behind the modulus trends for the <110> axially oriented nanowires in Figure 4.4a. It is clear that some combination of core nonlinearity and pure surface elasticity causes the observed increase in Young's modulus, but it is difficult to separate the two effects because there are no clear increasing or decreasing trends in modulus percent difference (Figure 4.5) for the bending and tension simulations. It is interesting to note, however, that the smallest rhombic nanowire shows a much higher modulus difference in tension and bending than the larger rhombic nanowires, whereas the square <110> wires do not show a significant difference in modulus values in bending and tension over the size range tested. The rhombic nanowires are laterally bound by {111} surfaces; these low-energy surfaces have been shown to be slightly stiffer than the bulk along the <110> direction.[120] This surface stiffness could give rise to the observed bending and tension modulus difference for the smallest rhombic nanowire due to preferential sampling of the surface in bending. In addition, stress concentrations at the upper and lower corners in rhombic nanowires under bending loads could play a role in this modulus increase. Other than in the smallest rhombic nanowire, the differences in bending and tension for these nanowires are not as pronounced as in the <100> axially oriented nanowires.

4.4 Summary and conclusions

In summary, molecular statics simulations have been carried out to determine the elastic properties of silver nanowires under both bending and tensile loads. An

incremental loading method was developed to simulate bending and was applied to nanowires of varying size, geometry, and surface orientation. The Young's modulus was calculated for each nanowire under both loading conditions by using strain energy methods derived from continuum mechanics. The modulus values for nanowires with a <110> axial orientation were observed to increase with decreasing cross-sectional thickness, while the modulus values for nanowires with a <100> axial orientation were observed to decrease with decreasing cross-sectional thickness. This behavior is in accordance with previous studies involving nanowire elastic properties, and it can be attributed to the nonlinear elasticity of the nanowire core and dissimilar surface and core elastic modulus values. For <100> axially oriented nanowires, surface elasticity is observed to play a larger role in bending simulations than in tensile simulations in determining the nanowire elastic modulus because of preferential sampling of the surfaces elasticity in bending. For the <110> axially oriented nanowires, the observed modulus increase with decreasing size is consistent with predictions based on core nonlinear elasticity, but it is difficult to separate the surface elasticity and core nonlinearity effects as in the <100> nanowires because of a lack of clear trends.

Overall, this study shows that continuum mechanics models give quantitatively similar results for the elastic modulus of nanowires under bending and tensile loading conditions, especially for larger wires. This is comforting in that it serves to bridge the gap between commonly used experimental and computational techniques (bending and tension, respectively). In these simulations, the effects of loading method on elastic modulus become significant only in wires with cross-sectional thicknesses below about 5 nm, which is significantly smaller than the current experimental size range. Either of the

loading methods should yield similar results for nanowires of larger sizes.

Although this study illuminates the differences and similarities in bending and tension for determination of the elastic properties of silver nanowires, it must be emphasized that these results are for single crystal, defect free, pure silver nanowires. Experimental studies of nanowire elasticity usually focus on larger nanowires, and there are many factors that could cause changes in elasticity that are not present in simulations. This work has taken a step in comparing nanowire experiments and simulations by using different loading methods, but further research is needed to fully determine the true nature of metal nanowire elasticity.

CHAPTER V

ENERGY LANDSCAPES OF DEFORMATION IN METAL NANOWIRES

5.1 Introduction

In the most basic form, the ground state, total energy of a metallic face-centered-cubic (FCC) nanowire may be considered as the sum of core, surface, and edge components. In the ideal case, atoms in the core of the nanowire are fully coordinated and possess a cohesive energy approximately equivalent to the bulk value. This energy is essentially isotropic; the electron gas surrounding a central atom is equally dispersed among its twelve nearest neighbor atoms. In contrast, atoms comprising the free surfaces and edges are under-coordinated, and thus increase the total energy of the nanowire, since in metallic bonding the density of the electron gas is tightly coupled with the atomic coordination. For a particular element, there exists an ideal electron density that minimizes the energy of an individual atom. Any variation in the electron density from the ideal value results in an increase in the energy of the atom. Under-coordination of an atom causes an increase in energy due to increased electrostatic attraction, whereas over-coordination results in excessive repulsive energy on the central atom. The degree of under-coordination of an atom on a surface or edge relative to an atom in the nanowire core is dependent on the crystallographic orientation of the free surface, which is defined by the normal to the surface plane. For this reason, the surface and edge energies are anisotropic. In order to approach the ideal, energy minimizing electron density, surface

atoms contract towards the nanowire core thus imposing a compressive surface stress on the core of the nanowire. As the cross-sectional dimensions of a nanowire are reduced, the surface area to volume ratio is amplified, and the relative contribution of the surface and edge energies to the total energy of the nanowire increases accordingly. This is depicted in Figure 5.1.

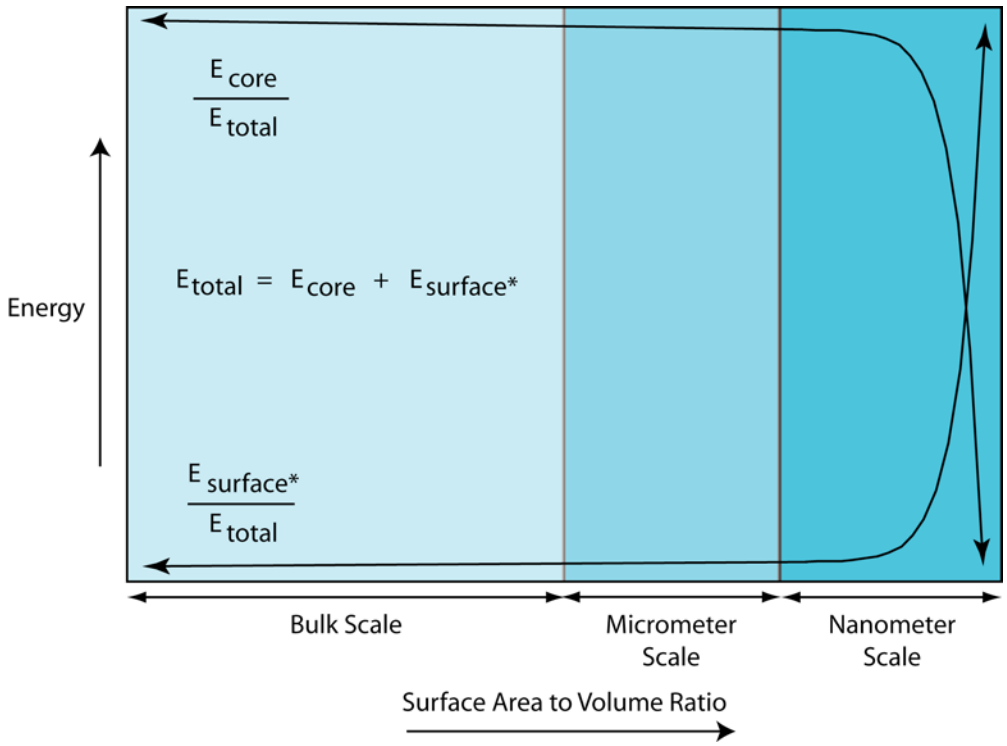

Figure 5.1: The contribution of surface and core atoms to the total energy of a material as a function of length scale. Surfaces are defined as facets of a specific orientation and edges are the entity formed from the intersection of facets of differing orientation. Core atoms are considered as fully coordinated atoms beneath the surface of the material.

At a critical length in the nanometer scale regime in Figure 5.1, there exists a crossover where the total energy of the material is more strongly affected by the excess energy from the free surfaces than of the core energy. The magnitude of surface energy is

dependent on the crystallographic orientation of the surface. For FCC materials, the close packed {111} surfaces exhibit the lowest surface energy, followed by {100} surfaces and then {110} type surfaces. Thus, the total energy of a material is dependent on not only on the surface-area-to-volume ratio, but also on the crystallographic orientation of the free surfaces.

Many researchers have determined that the mechanical behavior of metal nanowires is modified from surface effects. Size dependence of mechanical properties has been revealed for the elastic modulus, the torsional rigidity, and the yield strength of nanowires. Recently, it has been shown that the operant deformation mechanisms in metal nanowires are strongly dependent on the crystallographic properties of the nanowire. Park et al conducted a systematic study on metal nanowires with varying axial and surface orientation to examine the deformation mechanisms responsible for incipient plasticity. Their results showed that metal nanowires with a <100> axial orientation and {100} side surfaces plastically deformed under tension by the motion of full and partial dislocations along the length of the nanowire, while the compression of <100> axially oriented nanowires with {110} surfaces resulted in deformation solely by the motion of partial dislocations. In Chapter 3, we presented results on the tensile deformation of <110> oriented nanowires, and showed that for three different nanowire geometries, with different free surface orientations and cross sectional geometry, the operant deformation mechanisms was strongly dependent on the nanowire geometry. An interesting outcome of this work was related to the deformation of rhombic and truncated rhombic <110> oriented nanowires.

The rhombic nanowires (as shown previously in Figure 3.2a) exhibit a <110> axial orientation and all free surfaces are bound by low energy {111} planes. The truncated-rhombic nanowires (as shown in Figure 3.2b) are created by slicing a set of vertices of the rhombic wire, to expose {100} surfaces in addition to the {111} surfaces. It was discovered that the tensile loading of perfect rhombic wires resulted in plastic deformation through the process of deformation twinning, while the truncated-rhombic nanowires deformed by the organized motion of partial dislocations along the length of the nanowire.

This work aims to understand why the operant deformation mechanisms in these two nanowires differ. Since the nanowires exhibit the same axial orientation, but different surface orientations, they are an ideal case to analyze the effect of surface orientation on deformation behavior. We have developed a technique to determine the energy landscape for various deformation pathways in nanowires. Using this technique, we have performed a systematic analysis of the deformation of rhombic silver nanowires with a varying extent of truncation, and discovered a crossover in the operant deformation mechanism, depending solely on the amount of exposed {100} surfaces of the nanowire. In addition, we show in this work, that truncated nanowires may also deform by deformation twinning, and reorient themselves into a new crystallographic orientation and surface structure.

5.2 Simulation methodology

The simulations in this work utilize both MD and MS calculations using the EAM, as outlined in Chapter 2. All simulations are conducted using the Voter and Chen EAM potential for silver, the details of which are also presented in Chapter 2. We have

performed MD simulations order to deduce the operant deformation mechanisms in rhombic nanowires of varying truncation. With knowledge of the operant mechanisms, we then performed MS calculations to map the energetic landscape during the initial deformation process. In this section, the nanowire geometries considered will be presented, and the MD and MS simulation procedures will be explained.

5.2.1 Nanowire geometries

The nanowire geometries considered in this analysis are shown in Figure 5.2. The nanowires are representative of experimentally observed nanowire geometries for silver. In addition, these nanowire geometries are predicted to be energetically favorable, as compared to other geometric possibilities. We have considered five different rhombic nanowires and truncated-rhombic nanowires, with varying extents of truncation. During the truncation of a perfect rhombic nanowire, {100} surfaces are exposed. For increasing levels of truncation (*n=1* to *n=4* in Figure 5.2), the surface area of the {100} surfaces is increased. The nanowires have a finite length, of approximately 18 nanometers, in the <110> direction. In this work, the size of the perfect rhombic nanowire in Figure 5.2a was 2.2 nm. We did not consider other sizes for the starting point of truncation.

5.2.2 Molecular dynamics procedures

MD simulations were used in this work to observe the operant deformation mechanisms in the nanowires. The nanowires were loaded under tension at a uniform strain rate of 10^8 s^{-1}. The loading was performed using the continuous dynamic loading procedure introduced in Chapter 2, and described in detail in Chapter 3. This procedure will not be described in this section. During the tensile deformation, the centrosymmetry

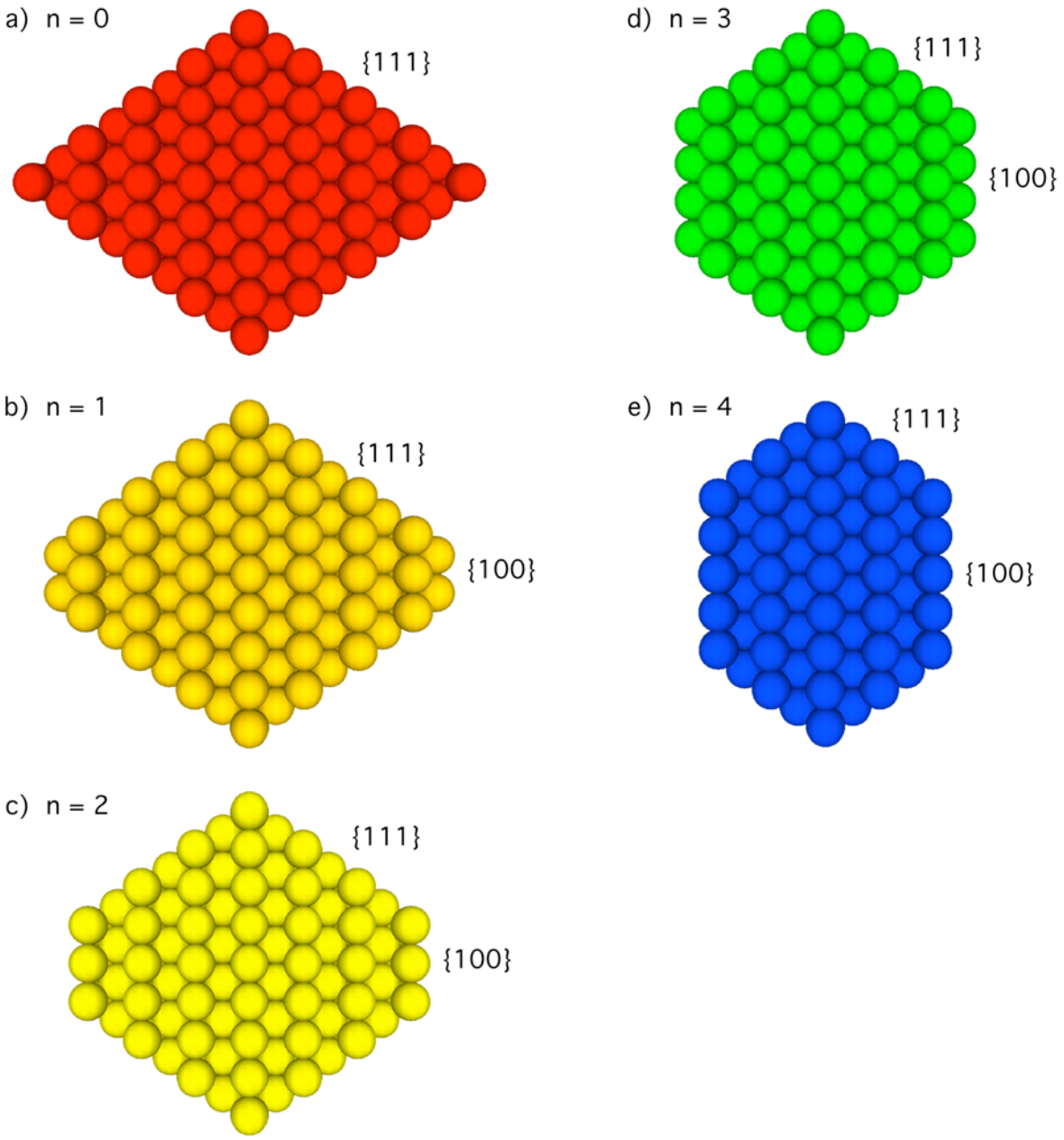

Figure 5.2: Snapshots of the cross-sectional geometry and crystallographic structure of the rhombic and truncated nanowire geometries considered in this work. A perfect rhombic nanowire (*n=0*) is shown in (a), and each subsequent cross-section is labeled according to the extent of truncation, where *n* represents the number of atomic layers removed relative to a perfect rhombic nanowire during the truncation. The surface orientation is indicated for each nanowire and all nanowires are axially oriented in the <110> direction.

of all atoms was monitored so that defects could be easily identified during the post-processing of results.

The MD simulations of tensile deformation reveal two primary mechanisms of deformation in the rhombic-type silver nanowires. These are deformation twinning and partial dislocation mediated slip. For the remainder of this chapter, these deformation pathways will be referred to as twinning and slip, respectively. These mechanisms were presented in detail in Chapter 3: twinning was presented in section 3.3.1 and slip was discussed in 3.3.2.

5.2.3 Molecular statics procedures

The MS simulations in this work were used in order to track the system energy during the initial deformation of the nanowires. The observed deformation behavior from the MD simulations, twinning and slip, was reproduced in the MS simulations by applying displacements along appropriate slip planes in the nanowire. This procedure is very similar to the one used to generate the GSF curves, as discussed in section 2.7.1. The first step in reproducing the deformation observed in the dynamic simulations is the minimization of the system energy. This assures that the nanowire is in equilibrium, and that atoms near the surface have 'relaxed' towards the nanowire core. Next, the deformation pathways of twinning and slip are imposed on the nanowires. Since the purpose of the MS simulations is to deduce *why* specific deformation mechanisms occur, both twinning and slip are simulated for each nanowire geometry, in order to map out the energy during deformation (even though from the dynamic simulations it is evident that one mechanism is energetically favored over the other). The deformation processes are described in detail below.

5.2.4 Deformation pathways

The atomic configurations for the deformation pathways of twinning and slip are presented in Figures 5.3 and 5.4. The first step for both the twinning and slip deformation pathways is to generate a stacking fault in the nanowire. This is achieved by displacing two slip planes past one another, incrementally, along the <112> direction on the slip plane. The atomic configurations for the formation of a stacking fault in the nanowires are presented in Figures 5.3a-c and 5.4a-c for twinning and slip, respectively.

After the formation of the initial stacking fault, the deformation pathways for twinning and slip diverge. For deformation twinning, the initial stacking fault dissociates into a twin fault pair, leaving behind a reoriented portion of the nanowire in the process. This process is illustrated in Figure 5.3d,e. The slip process involves the formation of additional stacking faults on both sides of the initial stacking fault, and in the process forms a 'zig-zag' stacking fault network. The atomic configurations for the formation of the stacking fault network are displayed in Figure 5.4d,e.

Since the deformation pathways for twinning and slip are initially the same, the energetic response for a specific nanowire undergoing each process will be the same up until the formation of the initial stacking fault. However, the energetic landscape for the processes thereafter will differ, and one pathway should prove to be energetically favorable over the other. Thus it is necessary to track the system energy during each deformation process to determine which is energetically favored. The process to obtain the energy is straightforward and not computationally intensive. At each displacement increment, after applying the displacement to the appropriate atoms, the positions of all atoms in the simulation are fixed, and the system energy is minimized using the iterative

conjugate gradient solver. Since the positions of all atoms are constrained, the conjugate gradient solver only requires a single iteration, and the energy of the system is easily calculated. The potential energy after each displacement increment is subtracted from the initial, equilibrium system energy (calculated from the initial energy minimization, prior to deformation), and then is divided by the surface area of the slip plane in the nanowire. The energy per unit area is then plotted as a function of the displacement along the <112> direction of the slip plane.

5.3 Results

This section will summarize the observed deformation mechanisms in the dynamic simulations, as well as present the energetic landscapes for the two deformation pathways in the rhombic-type nanowires.

5.3.1 Operant deformation mechanisms

From the dynamic tensile deformation simulations, it was determined that for truncated-rhombic nanowires with $n \leq 3$, the operant deformation mechanism is twinning, while for the n=4 nanowire the operant mechanism was partial dislocation mediated slip. Deformation twinning in the n=0 nanowires has been reported previously, both in this work, and also as the reversible mechanism responsible for the shape memory effect in metal nanowires. However, the occurrence of deformation twinning in truncated-rhombic nanowires has not been previously presented.

As mentioned previously, deformation twinning results in a lattice reorientation. In nanowires with an initial <110> axial orientation, as is the case in this work, the lattice is reoriented to the <100> direction. In order to accommodate the reorientation of the

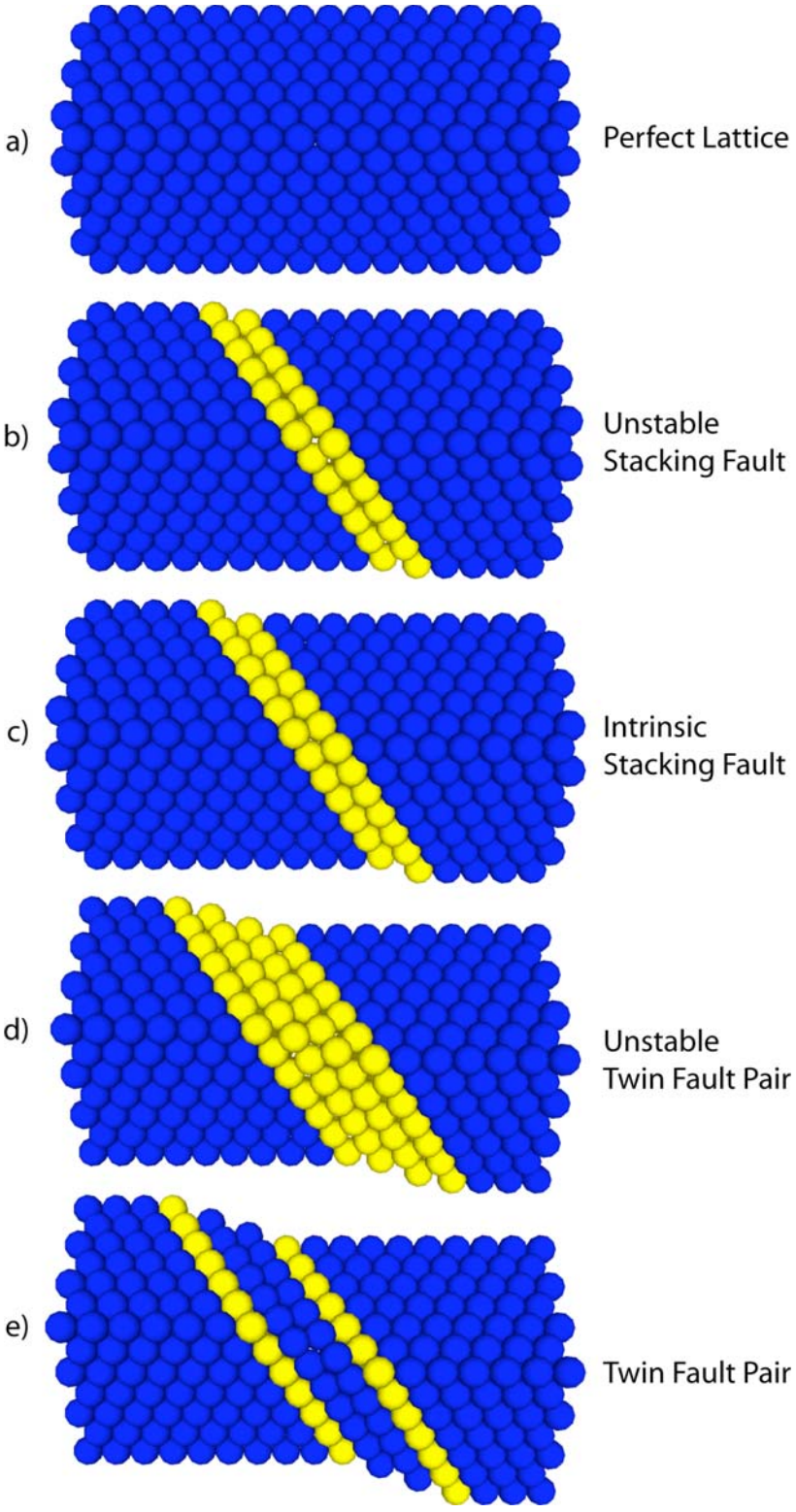

Figure 5.3: Atomic configurations for a perfect rhombic nanowire undergoing the process of deformation twinning.

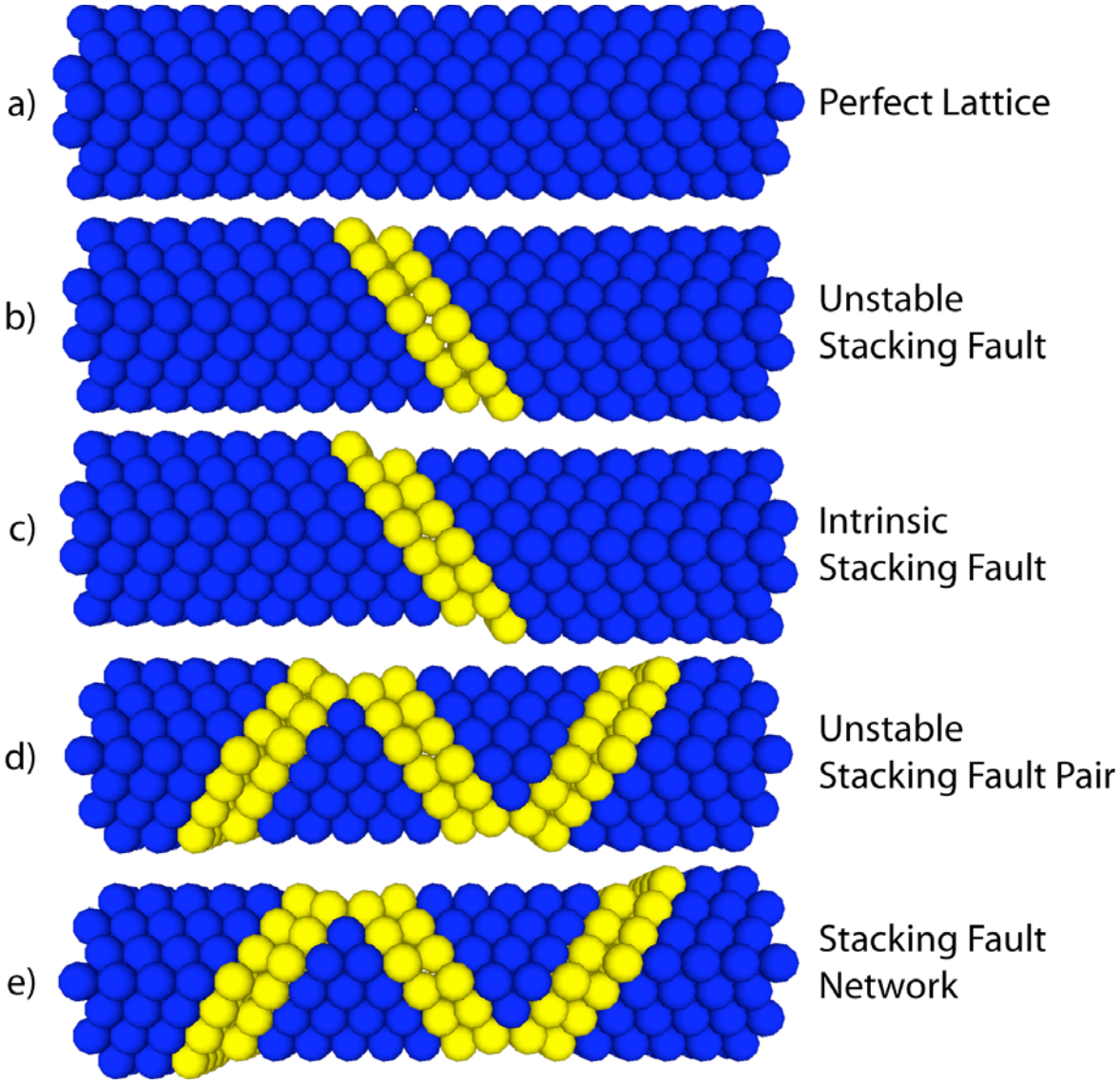

Figure 5.4: Atomic configurations for a truncated-rhombic nanowire undergoing the process of partial dislocation slip, and forming a zig-zag network of stacking faults along the length of the nanowire.

nanowire axis, the free surfaces must also reorient themselves. For the perfect rhombic (n = 0) nanowires, the {111} surfaces are reoriented to a {100} orientation. For the truncated-rhombic nanowires ($1 \leq n \leq 3$) in which there are both {111} and {100} free surfaces, initially, the surfaces are reoriented to {100} and {110}, respectively. The

crystallographic structure of undeformed and reoriented perfect rhombic and truncated-rhombic nanowires is presented in Figure 5.5.

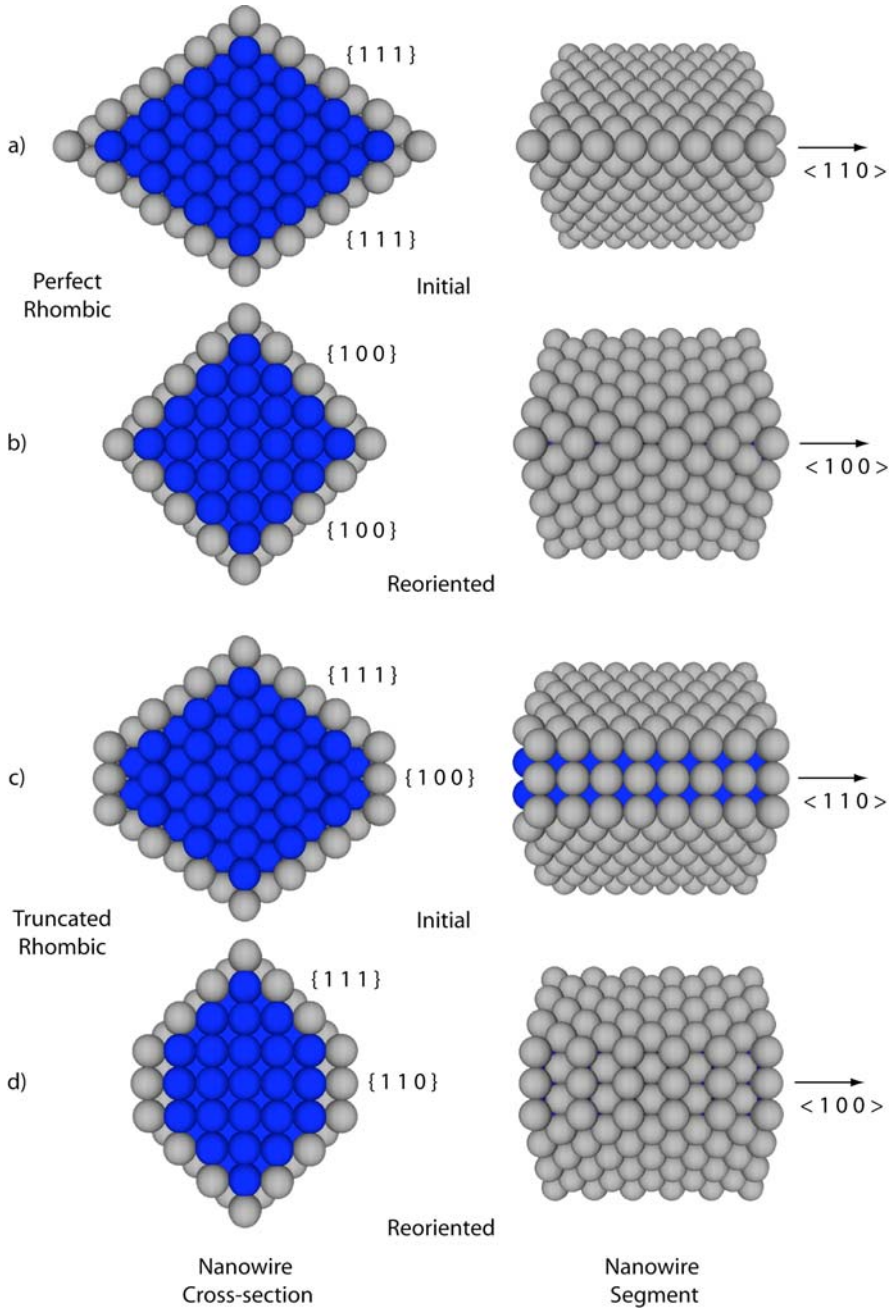

Figure 5.5: Structure and geometry of rhombic (a,b) and truncated-rhombic (c,d) silver nanowires before (a,c) and after (b,d) undergoing the process of deformation twinning.

5.3.2 Energy landscapes of twinning and slip

The energy landscapes of the twinning and slip deformation pathways for all the nanowire geometries presented in Figure 5.2 is shown below in Figure 5.6. From this figure, several trends are observed. The energetic barrier to forming the initial stacking fault occurs at a displacement of approximately 1 Å. This energetic barrier is comparable to the unstable stacking fault energy. It is apparent that this energetic barrier increases with increasing truncation. At a displacement of around 1.6 Å, the initial stacking fault is formed, and the nanowires are essentially in a metastable equilibrium state. After the

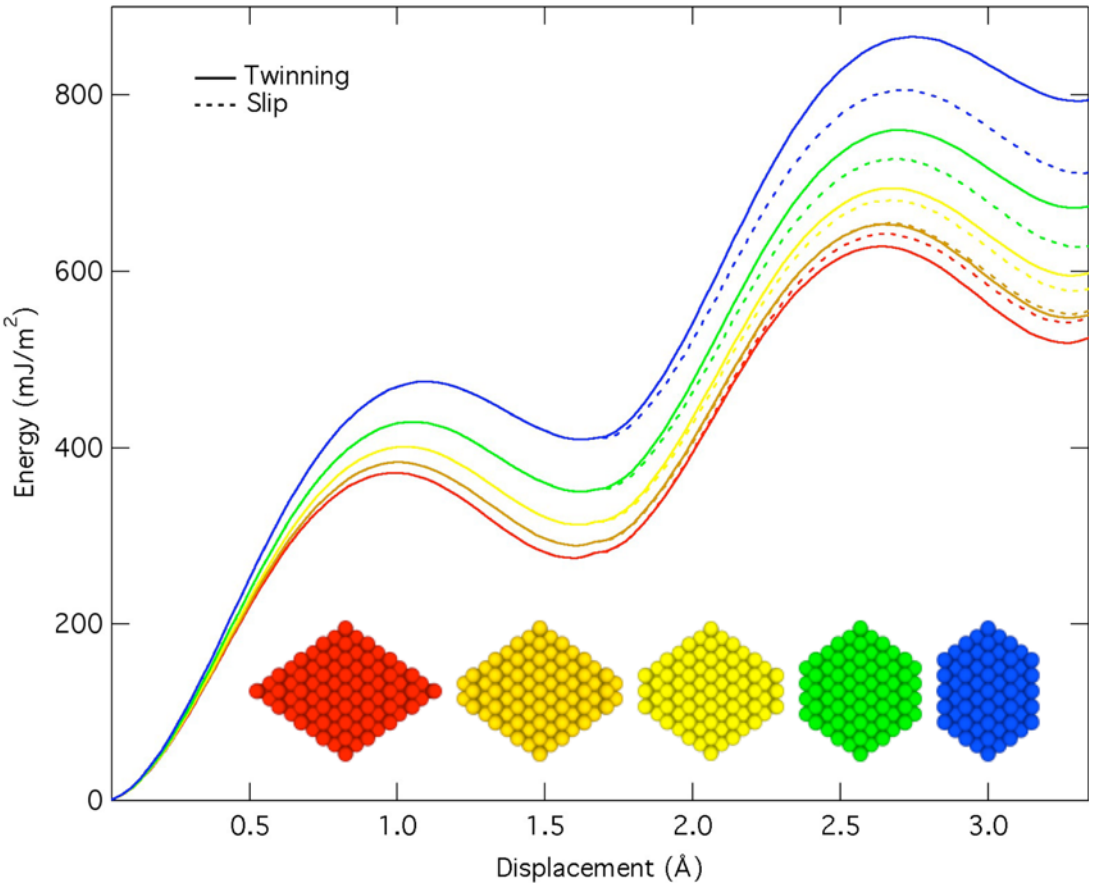

Figure 5.6: Energy landscapes for twinning and slip in rhombic and truncated-rhombic silver nanowires. The energy curves correspond to the color of each cross-section shown (inset). The energetic pathway for twinning is shown as a solid line, and the energetic pathway for slip is shown as a dashed line.

formation of the initial stacking fault, the deformation pathways diverge from a common path, and the energetically favorable deformation pathways are revealed for each geometry. For each of these pathways, a second energy barrier must be overcome in order to form the next metastable defect configuration. The energetically favored deformation pathway will be the pathway that has a lower energetic barrier during the deformation process. For the n=0 and n=1 the favored deformation pathway is twinning, since the twinning curve lies below the slip curve for each of these geometries. For the truncated-rhombic nanowires in which $1 < n \leq 4$, the energetically favorable pathway is revealed to be slip. It is also apparent that the difference in the energetic barriers of twinning and slip increases with increasing truncation.

5.4 Discussion

The nanowires considered in this work differ only in the overall composition of the free surfaces, yet they are predicted to deform by different deformation mechanisms. The energetically favorable deformation mechanism must therefore be dictated by the orientation of the free surfaces. To understand why one deformation pathway is energetically favored over the other, it is helpful to first discuss the present the energies of FCC surfaces, then to examine the change in atomic configuration during the deformation process, for each deformation pathway.

To aid in this analysis of the results presented in this work, we calculated the surface energies of the three low-index surfaces for FCC silver, as predicted by the Voter-Chen EAM potential for silver. These values are summarized in Table 5.1 below.

Table 5.1: Surface energies for the low-index surfaces of silver as calculated from the Voter-Chen EAM potential.

Surface Orientation	Surface Energy (mJ/m^2)
{111}	802.9
{100}	879.7
{110}	1313.3

During the deformation twinning process, the free surfaces are reoriented from {111} to {100} and from {100} to {110}. Since for both initial surface orientations, the reoriented surface exhibits a *higher* surface energy, there is an energetic penalty associated with the reorientation process. The penalty for reorienting a {111} free surface of a given area to a {100} surface is on the order of 75 *mJ*, while the penalty for converting a {100} surface to a {110} orientation is 433.6 *mJ*. These values can be related to the energetic barrier that must be overcome during the twinning process. As the truncation of the perfect rhombic nanowire is increased, a larger area of {100} surfaces is exposed, at the sacrifice of lower energy {111} surfaces. Since the energetic penalty for reorienting {100} surfaces is much higher than that to reorient {111} surfaces, the energetic barrier for the twinning deformation pathway increases with increasing truncation.

During the slip process, no lattice reorientation occurs. The energy that is added to the system in this deformation pathway is a result of the imperfect stacking arrangement in the lattice and the inhomogeneity created at the free surface from the stacking fault. The energetic barrier for this process also changes with increasing truncation, but not as drastically as it does during for the deformation twinning pathway.

Thus, a crossover in operant deformation mechanisms is predicted, because for a given level of truncation, the energetic barrier presented by the reorientation of {100} free surfaces to a {110} orientation exceeds that of the formation of a stacking fault network in the nanowire. The dynamic simulations agree quite well with the static calculations, however, in the dynamic simulations, the n=3 nanowire was predicted to undergo slip rather than deformation twinning as predicted from the MS energy calculations. We achieve this difference to the influence of thermal activation during the deformation process in dynamic simulations.

5.5 Conclusions

In this work, we have presented a systematic analysis of the operant deformation mechanisms in top-down rhombic-type silver nanowires, as a function of truncation. Simulations were conducted to examine the effect of free surface orientation on the deformation behavior in order to determine the energetically favored deformation pathway for each nanowire geometry. A new technique was developed to maps out the energy landscape of the twinning and slip deformation pathways in metal nanowires using MS procedures. It was determined that the energetic penalties from surface reorientation during deformation twinning dictates which deformation pathway (twinning or slip) will be energetically favored. It was determined that for a specific free surface composition (n=2), slip is the energetically favored deformation pathway. While this finding is specific to silver and the chosen starting diameter of the n=0 nanowire, this method may be easily extended to other nanowire geometries and deformation pathways in order to understand the influence of free surfaces on deformation behavior.

REFERENCES

[1] M. A. El-Sayed, Some interesting properties of metals confined in time and nanometer space of different shapes, *Accounts of Chemical Research* **2001**, *34*, 257-264.

[2] M. C. Daniel, D. Astruc, Gold nanoparticles: Assembly, supramolecular chemistry, quantum-size-related properties, and applications toward biology, catalysis, and nanotechnology, *Chemical Reviews* **2004**, *104*, 293-346.

[3] Y. N. Xia, P. D. Yang, Y. G. Sun, Y. Y. Wu, B. Mayers, B. Gates, Y. D. Yin, F. Kim, Y. Q. Yan, One-dimensional nanostructures: Synthesis, characterization, and applications, *Advanced Materials* **2003**, *15*, 353-389.

[4] Y. Huang, X. F. Duan, Y. Cui, L. J. Lauhon, K. H. Kim, C. M. Lieber, Logic gates and computation from assembled nanowire building blocks, *Science* **2001**, *294*, 1313-1317.

[5] Y. Huang, X. F. Duan, Q. Q. Wei, C. M. Lieber, Directed assembly of one-dimensional nanostructures into functional networks, *Science* **2001**, *291*, 630-633.

[6] N. I. Kovtyukhova, T. E. Mallouk, Nanowires as building blocks for self-assembling logic and memory circuits, *Chemistry-a European Journal* **2002**, *8*, 4355-4363.

[7] S. A. Maier, M. L. Brongersma, P. G. Kik, S. Meltzer, A. A. G. Requicha, H. A. Atwater, Plasmonics - A route to nanoscale optical devices, *Advanced Materials* **2001**, *13*, 1501-+.

[8] S. A. Maier, P. G. Kik, H. A. Atwater, S. Meltzer, E. Harel, B. E. Koel, A. A. G. Requicha, Local detection of electromagnetic energy transport below the diffraction limit in metal nanoparticle plasmon waveguides, *Nature Materials* **2003**, *2*, 229-232.

[9] H. Y. Fan, Y. F. Lu, A. Stump, S. T. Reed, T. Baer, R. Schunk, V. Perez-Luna, G. P. Lopez, C. J. Brinker, Rapid prototyping of patterned functional nanostructures, *Nature* **2000**, *405*, 56-60.

[10] H. J. Gao, B. H. Ji, I. L. Jager, E. Arzt, P. Fratzl, Materials become insensitive to flaws at nanoscale: Lessons from nature, *Proceedings of the National Academy of Sciences of the United States of America* **2003**, *100*, 5597-5600.

[11] B. H. Ji, H. J. Gao, Mechanical properties of nanostructure of biological materials, *Journal of the Mechanics and Physics of Solids* **2004**, *52*, 1963-1990.

[12] E. Katz, I. Willner, Integrated nanoparticle-biomolecule hybrid systems: Synthesis, properties, and applications, *Angewandte Chemie-International Edition* **2004**, *43*, 6042-6108.

[13] D. A. Schultz, Plasmon resonant particles for biological detection, *Current Opinion in Biotechnology* **2003**, *14*, 13-22.

[14] A. K. Salem, P. C. Searson, K. W. Leong, Multifunctional nanorods for gene delivery, *Nature Materials* **2003**, *2*, 668-671.

[15] Y. Kondo, K. Takayanagi, Synthesis and characterization of helical multi-shell gold nanowires, *Science* **2000**, *289*, 606-608.

[16] Y. Kondo, K. Takayanagi, Gold nanobridge stabilized by surface structure, *Physical Review Letters* **1997**, *79*, 3455-3458.

[17] K. K. Caswell, C. M. Bender, C. J. Murphy, Seedless, surfactantless wet chemical synthesis of silver nanowires, *Nano Letters* **2003**, *3*, 667-669.

[18] Y. Gao, P. Jiang, L. Song, L. F. Liu, X. Q. Yan, Z. Q. Zhou, D. F. Liu, J. X. Wang, H. J. Yuan, Z. X. Zhang, X. W. Zhao, X. Y. Dou, W. Y. Zhou, G. Wang, S. S. Xie, Growth mechanism of silver nanowires synthesized by polyvinylpyrrolidone-assisted polyol reduction, *Journal of Physics D-Applied Physics* **2005**, *38*, 1061-1067.

[19] C. Y. Ni, P. A. Hassan, E. W. Kaler, Structural characteristics and growth of pentagonal silver nanorods prepared by a surfactant method, *Langmuir* **2005**, *21*, 3334-3337.

[20] G. Sauer, G. Brehm, S. Schneider, K. Nielsch, R. B. Wehrspohn, J. Choi, H. Hofmeister, U. Gosele, Highly ordered monocrystalline silver nanowire arrays, *Journal of Applied Physics* **2002**, *91*, 3243-3247.

[21] T. Scheibel, R. Parthasarathy, G. Sawicki, X. M. Lin, H. Jaeger, S. L. Lindquist, Conducting nanowires built by controlled self-assembly of amyloid fibers and selective metal deposition, *Proceedings of the National Academy of Sciences of the United States of America* **2003**, *100*, 4527-4532.

[22] Y. G. Sun, B. Mayers, T. Herricks, Y. N. Xia, Polyol synthesis of uniform silver nanowires: A plausible growth mechanism and the supporting evidence, *Nano Letters* **2003**, *3*, 955-960.

[23] Y. G. Sun, Y. N. Xia, Large-scale synthesis of uniform silver nanowires through a soft, self-seeding, polyol process, *Advanced Materials* **2002**, *14*, 833-837.

[24] N. R. Jana, L. Gearheart, C. J. Murphy, Seed-mediated growth approach for shape-controlled synthesis of spheroidal and rod-like gold nanoparticles using a surfactant template, *Advanced Materials* **2001**, *13*, 1389-1393.

[25] C. J. Murphy, N. R. Jana, Controlling the aspect ratio of inorganic nanorods and nanowires, *Advanced Materials* **2002**, *14*, 80-82.

[26] J. R. Greer, W. C. Oliver, W. D. Nix, Size dependence of mechanical properties of gold at the micron scale in the absence of strain gradients, *Acta Materialia* **2005**, *53*, 1821-1830.

[27] P. E. Marszalek, W. J. Greenleaf, H. B. Li, A. F. Oberhauser, J. M. Fernandez, Atomic force microscopy captures quantized plastic deformation in gold nanowires, *Proceedings of the National Academy of Sciences of the United States of America* **2000**, *97*, 6282-6286.

[28] M. S. Daw, S. M. Foiles, M. I. Baskes, The Embedded-Atom Method - a Review of Theory and Applications, *Materials Science Reports* **1993**, *9*, 251-310.

[29] J. Diao, Gall, K., and M. L. Dunn, Surface-stress-induced phase transformation in metal nanowires, *Nature Materials* **2003**, *2*, 656-660.

[30] J. Diao, Gall, K., and M. L. Dunn, Surface stress driven reorientation of gold nanowires, *Physical Review B* **2004**, *70*, 075413.

[31] J. Diao, Gall, K., Dunn, M. L., and J. A. Zimmerman, Atomistic simulations of the yielding of gold nanowires, *Acta Materialia* **2006**, *54*, 643-653.

[32] J. K. Diao, K. Gall, M. L. Dunn, Yield strength asymmetry in metal nanowires, *Nano Letters* **2004**, *4*, 1863-1867.

[33] K. Gall, Diao, J., and M. L. Dunn, The Strength of Gold Nanowires, *Nano Letters* **2004**, *4*, 2431-2436.

[34] K. Gall, J. K. Diao, M. L. Dunn, The strength of gold nanowires, *Nano Letters* **2004**, *4*, 2431-2436.

[35] B. Hyde, H. D. Espinosa, D. Farkas, An atomistic investigation of elastic and plastic properties of Au nanowires, *Jom* **2005**, *57*, 62-66.

[36] H. S. Park, Gall, K., and J.A. Zimmerman, Deformation of FCC Nanowires by Twinning and Slip, *J. Mechanics and Physics of Solids* **2005**.

[37] H. S. Park, and C. Ji, On the Thermomechanical Deformation of Silver Shape Memory Nanowires, *Acta Materialia* **2006**.

[38] A. M. Leach, M. McDowell, K. Gall, Deformation of Top-Down and Bottom-Up Silver Nanowires, *Advanced Functional Materials, In Press.*

[39] H. S. Park, K. Gall, J. A. Zimmerman, Deformation of FCC nanowires by twinning and slip, *Journal of the Mechanics and Physics of Solids* **2006**, *54*, 1862-1881.

[40] I. N. Levine, *Quantum Chemistry*, Prentice-Hall, Upper Saddle River, New Jersey **2000**.

[41] W. G. Hoover, Canonical Dynamics - Equilibrium Phase-Space Distributions, *Physical Review A* **1985**, *31*, 1695-1697.

[42] S. Nose, A Unified Formulation of the Constant Temperature Molecular-Dynamics Methods, *Journal of Chemical Physics* **1984**, *81*, 511-519.

[43] D. a. S. Frenkel, B., *Understanding Molecular Simulation: From Algorithms to Applications*, Academic Press, San Diego **2002**.

[44] M. S. Daw, M. I. Baskes, Embedded-Atom Method - Derivation and Application to Impurities, Surfaces, and Other Defects in Metals, *Physical Review B* **1984**, *29*, 6443-6453.

[45] K. W. Jacobsen, J. K. Norskov, M. J. Puska, Interatomic Interactions in the Effective-Medium Theory, *Physical Review B* **1987**, *35*, 7423-7442.

[46] K. W. Jacobsen, P. Stoltze, J. K. Norskov, A semi-empirical effective medium theory for metals and alloys, *Surface Science* **1996**, *366*, 394-402.

[47] M. I. Baskes, Application of the Embedded-Atom Method to Covalent Materials - a Semiempirical Potential for Silicon, *Physical Review Letters* **1987**, *59*, 2666-2669.

[48] M. I. Baskes, Modified Embedded-Atom Potentials for Cubic Materials and Impurities, *Physical Review B* **1992**, *46*, 2727-2742.

[49] M. I. Baskes, Determination of modified embedded atom method parameters for nickel, *Materials Chemistry and Physics* **1997**, *50*, 152-158.

[50] M. I. Baskes, R. A. Johnson, Modified Embedded-Atom Potentials for Hcp Metals, *Modelling and Simulation in Materials Science and Engineering* **1994**, *2*, 147-163.

[51] A. F. Voter, **1993**.

[52] H. S. Park, J. A. Zimmerman, Modeling inelasticity and failure in gold nanowires, *Physical Review B* **2005**, *72*, 054106.

[53] H. S. Park, J. A. Zimmerman, Stable nanobridge formation in < 1 1 0 > gold nanowires under tensile deformation, *Scripta Materialia* **2006**, *54*, 1127-1132.

[54] J. A. Zimmerman, H. J. Gao, F. F. Abraham, Generalized stacking fault energies for embedded atom FCC metals, *Modelling and Simulation in Materials Science and Engineering* **2000**, *8*, 103-115.

[55] H. Saka, Y. Sueki, T. Imura, Intrinsic Temperature-Dependence of Stacking-Fault Energy in Copper-Aluminium Alloys, *Philosophical Magazine a-Physics of Condensed Matter Structure Defects and Mechanical Properties* **1978**, *37*, 273-289.

[56] H. Suzuki, C. S. Barrett, Deformation Twinning in Silver-Gold Alloys, *Acta Metallurgica* **1958**, *6*, 156-165.

[57] N. Silvis-Cividjian, C. W. Hagen, P. Kruit, M. A. J. Van der Stam, H. B. Groen, Direct fabrication of nanowires in an electron microscope, *Applied Physics Letters* **2003**, *82*, 3514-3516.

[58] S. Hu, A. Hamidi, S. Altmeyer, T. Koster, B. Spangenberg, H. Kurz, Fabrication of silicon and metal nanowires and dots using mechanical atomic force lithography, *Journal of Vacuum Science & Technology B* **1998**, *16*, 2822-2824.

[59] N. Kramer, H. Birk, J. Jorritsma, C. Schonenberger, Fabrication of Metallic Nanowires with a Scanning Tunneling Microscope, *Applied Physics Letters* **1995**, *66*, 1325-1327.

[60] C. N. R. Rao, F. L. Deepak, G. Gundiah, A. Govindaraj, Inorganic nanowires, *Progress in Solid State Chemistry* **2003**, *31*, 5-147.

[61] Z. Y. Tang, N. A. Kotov, One-dimensional assemblies of nanoparticles: Preparation, properties, and promise, *Advanced Materials* **2005**, *17*, 951-962.

[62] H. E. Boyer, *Atlas of Stress-Strain Curves*, ASM International, Metals Park, Ohio 44073, USA **1987**.

[63] N. Agrait, G. Rubio, S. Vieira, Plastic-Deformation of Nanometer-Scale Gold Connective Necks, *Physical Review Letters* **1995**, *74*, 3995-3998.

[64] A. Stalder, U. Durig, Study of plastic flow in ultrasmall Au contacts, *Journal of Vacuum Science & Technology B* **1996**, *14*, 1259-1263.

[65] J. K. Diao, K. Gall, M. L. Dunn, Surface-stress-induced phase transformation in metal nanowires, *Nature Materials* **2003**, *2*, 656-660.

[66] J. K. Diao, K. Gall, M. L. Dunn, Surface stress driven reorientation of gold nanowires, *Physical Review B* **2004**, *70*, 075413.

[67] J. K. Diao, K. Gall, M. L. Dunn, Atomistic simulation of the structure and elastic properties of gold nanowires, *Journal of the Mechanics and Physics of Solids* **2004**, *52*, 1935-1962.

[68] J. K. Diao, K. Gall, M. L. Dunn, J. A. Zimmerman, Atomistic simulations of the yielding of gold nanowires, *Acta Materialia* **2006**, *54*, 643-653.

[69] W. Liang, M. Zhou, Response of copper nanowires in dynamic tensile deformation, *Proceedings of the Institution of Mechanical Engineers Part C-Journal of Mechanical Engineering Science* **2004**, *218*, 599-606.

[70] W. W. Liang, M. Zhou, Pseudoelasticity of single crystalline Cu nanowires through reversible lattice reorientations, *Journal of Engineering Materials and Technology-Transactions of the Asme* **2005**, *127*, 423-433.

[71] W. W. Liang, M. Zhou, Atomistic simulations reveal shape memory of fcc metal nanowires, *Physical Review B* **2006**, *73*, 115409.

[72] W. W. Liang, M. Zhou, F. J. Ke, Shape memory effect in Cu nanowires, *Nano Letters* **2005**, *5*, 2039-2043.

[73] H. S. Park, K. Gall, J. A. Zimmerman, Shape memory and pseudoelasticity in metal nanowires, *Physical Review Letters* **2005**, *95*, 255504.

[74] H. S. Park, C. J. Ji, On the thermomechanical deformation of silver shape memory nanowires, *Acta Materialia* **2006**, *54*, 2645-2654.

[75] T. Kizuka, Atomic process of point contact in gold studied by time-resolved high-resolution transmission electron microscopy, *Physical Review Letters* **1998**, *81*, 4448-4451.

[76] V. Rodrigues, T. Fuhrer, D. Ugarte, Signature of atomic structure in the quantum conductance of gold nanowires, *Physical Review Letters* **2000**, *85*, 4124-4127.

[77] G. E. Tommei, F. Baletto, R. Ferrando, R. Spadacini, A. Danani, Energetics of fcc and decahedral nanowires of Ag, Cu, Ni, and C-60: A quenched molecular dynamics study, *Physical Review B* **2004**, *69*, 115426.

[78] J. Bettini, V. Rodrigues, J. C. Gonzalez, D. Ugarte, Real-time atomic resolution study of metal nanowires, *Applied Physics a-Materials Science & Processing* **2005**, *81*, 1513-1518.

[79] V. Rodrigues, J. Bettini, A. R. Rocha, L. G. C. Rego, D. Ugarte, Quantum conductance in silver nanowires: Correlation between atomic structure and transport properties, *Physical Review B* **2002**, *65*, 153402.

[80] H. Y. Chen, Y. Gao, H. C. Yu, H. R. Zhang, L. B. Liu, Y. G. Shi, H. F. Tian, S. S. Xie, J. Q. Li, Structural properties of silver nanorods with fivefold symmetry, *Micron* **2004**, *35*, 469-474.

[81] H. Y. Chen, Y. Gao, H. R. Zhang, L. B. Liu, H. C. Yu, H. F. Tian, S. S. Xie, J. Q. Li, Transmission-electron-microscopy study on fivefold twinned silver nanorods, *Journal of Physical Chemistry B* **2004**, *108*, 12038-12043.

[82] Y. Gao, L. Song, P. Jiang, L. F. Liu, X. Q. Yan, Z. P. Zhou, D. F. Liu, J. X. Wang, H. J. Yuan, Z. X. Zhang, X. W. Zhao, X. Y. Dou, W. Y. Zhou, G. Wang, S. S. Xie, H. Y. Chen, J. Q. Li, Silver nanowires with five-fold symmetric cross-section, *Journal of Crystal Growth* **2005**, *276*, 606-612.

[83] H. Hofmeister, S. A. Nepijko, D. N. Ievlev, W. Schulze, G. Ertl, Composition and lattice structure of fivefold twinned nanorods of silver, *Journal of Crystal Growth* **2002**, *234*, 773-781.

[84] J. Reyes-Gasga, J. L. Elechiguerra, C. Liu, A. Camacho-Bragado, J. M. Montejano-Carrizales, M. J. Yacaman, On the structure of nanorods and nanowires with pentagonal cross-sections, *Journal of Crystal Growth* **2006**, *286*, 162-172.

[85] C. Q. Chen, Y. Shi, Y. S. Zhang, J. Zhu, Y. J. Yan, Size dependence of Young's modulus in ZnO nanowires, *Physical Review Letters* **2006**, *96*, 075505.

[86] S. Cuenot, C. Fretigny, S. Demoustier-Champagne, B. Nysten, Surface tension effect on the mechanical properties of nanomaterials measured by atomic force microscopy, *Physical Review B* **2004**, *69*, 165410.

[87] G. Y. Jing, H. L. Duan, X. M. Sun, Z. S. Zhang, J. Xu, Y. D. Li, J. X. Wang, D. P. Yu, Surface effects on elastic properties of silver nanowires: Contact atomic-force microscopy, *Physical Review B* **2006**, *73*, 235409.

[88] B. Wu, A. Heidelberg, J. J. Boland, J. E. Sader, X. M. Sun, Y. D. Li, Microstructure-hardened silver nanowires, *Nano Letters* **2006**, *6*, 468-472.

[89] R. C. Cammarata, K. Sieradzki, Effects of Surface Stress on the Elastic-Moduli of Thin-Films and Superlattices, *Physical Review Letters* **1989**, *62*, 2005-2008.

[90] F. Ding, H. Li, J. L. Wang, W. F. Shen, G. H. Wang, Elastic deformation and stability in pentagonal nanorods with multiple twin boundaries, *Journal of Physics-Condensed Matter* **2002**, *14*, 113-122.

[91] R. Dingreville, J. M. Qu, M. Cherkaoui, Surface free energy and its effect on the elastic behavior of nano-sized particles, wires and films, *Journal of the Mechanics and Physics of Solids* **2005**, *53*, 1827-1854.

[92] R. E. Miller, V. B. Shenoy, Size-dependent elastic properties of nanosized structural elements, *Nanotechnology* **2000**, *11*, 139-147.

[93] F. H. Streitz, R. C. Cammarata, K. Sieradzki, Surface-Stress Effects on Elastic Properties .1. Thin Metal-Films, *Physical Review B* **1994**, *49*, 10699-10706.

[94] H. Y. Liang, M. Upmanyu, H. C. Huang, Size-dependent elasticity of nanowires: Nonlinear effects, *Physical Review B* **2005**, *71*, 241403.

[95] K. S. Cheung, S. Yip, Atomic-Level Stress in an Inhomogeneous System, *Journal of Applied Physics* **1991**, *70*, 5688-5690.

[96] M. Zhou, A new look at the atomic level virial stress: on continuum-molecular system equivalence, *Proceedings of the Royal Society of London Series a-Mathematical Physical and Engineering Sciences* **2003**, *459*, 2347-2392.

[97] D. Sander, Surface stress: implications and measurements, *Current Opinion in Solid State & Materials Science* **2003**, *7*, 51-57.

[98] M. F. Yu, O. Lourie, M. J. Dyer, K. Moloni, T. F. Kelly, R. S. Ruoff, Strength and breaking mechanism of multiwalled carbon nanotubes under tensile load, *Science* **2000**, *287*, 637-640.

[99] X. D. Bai, P. X. Gao, Z. L. Wang, E. G. Wang, Dual-mode mechanical resonance of individual ZnO nanobelts, *Applied Physics Letters* **2003**, *82*, 4806-4808.

[100] P. Poncharal, Z. L. Wang, D. Ugarte, W. A. de Heer, Electrostatic deflections and electromechanical resonances of carbon nanotubes, *Science* **1999**, *283*, 1513-1516.

[101] G. Feng, W. D. Nix, Y. Yoon, C. J. Lee, A study of the mechanical properties of nanowires using nanoindentation, *Journal of Applied Physics* **2006**, *99*.

[102] X. D. Li, H. S. Hao, C. J. Murphy, K. K. Caswell, Nanoindentation of silver nanowires, *Nano Letters* **2003**, *3*, 1495-1498.

[103] B. Wu, A. Heidelberg, J. J. Boland, Mechanical properties of ultrahigh-strength gold nanowires, *Nature Materials* **2005**, *4*, 525-529.

[104] A. Heidelberg, L. T. Ngo, B. Wu, M. A. Phillips, S. Sharma, T. I. Kamins, J. E. Sader, J. J. Boland, A generalized description of the elastic properties of nanowires, *Nano Letters* **2006**, *6*, 1101-1106.

[105] J. H. Song, X. D. Wang, E. Riedo, Z. L. Wang, Elastic property of vertically aligned nanowires, *Nano Letters* **2005**, *5*, 1954-1958.

[106] E. W. Wong, P. E. Sheehan, C. M. Lieber, Nanobeam mechanics: Elasticity, strength, and toughness of nanorods and nanotubes, *Science* **1997**, *277*, 1971-1975.

[107] J. P. Salvetat, A. J. Kulik, J. M. Bonard, G. A. D. Briggs, T. Stockli, K. Metenier, S. Bonnamy, F. Beguin, N. A. Burnham, L. Forro, Elastic modulus of ordered and disordered multiwalled carbon nanotubes, *Advanced Materials* **1999**, *11*, 161-165.

[108] S. Hoffmann, I. Utke, B. Moser, J. Michler, S. H. Christiansen, V. Schmidt, S. Senz, P. Werner, U. Gosele, C. Ballif, Measurement of the bending strength of vapor-liquid-solid grown silicon nanowires, *Nano Letters* **2006**, *6*, 622-625.

[109] J. P. Salvetat, G. A. D. Briggs, J. M. Bonard, R. R. Bacsa, A. J. Kulik, T. Stockli, N. A. Burnham, L. Forro, Elastic and shear moduli of single-walled carbon nanotube ropes, *Physical Review Letters* **1999**, *82*, 944-947.

[110] A. San Paulo, J. Bokor, R. T. Howe, R. He, P. Yang, D. Gao, C. Carraro, R. Maboudian, Mechanical elasticity of single and double clamped silicon nanobeams fabricated by the vapor-liquid-solid method, *Applied Physics Letters* **2005**, *87*.

[111] Y. X. Chen, B. L. Dorgan, D. N. McIlroy, D. E. Aston, On the importance of boundary conditions on nanomechanical bending behavior and elastic modulus determination of silver nanowires, *Journal of Applied Physics* **2006**, *100*.

[112] S. G. Nilsson, X. Borrise, L. Montelius, Size effect on Young's modulus of thin chromium cantilevers, *Applied Physics Letters* **2004**, *85*, 3555-3557.

[113] A. M. Leach, M. McDowell, K. Gall, Deformation of top-down and bottom-up silver nanowires, *Advanced Functional Materials* **2007**, *17*, 43-53.

[114] C. J. Ji, H. S. Park, Characterizing the elasticity of hollow metal nanowires, *Nanotechnology* **2007**, *18*.

[115] M. J. Buehler, H. M. Yao, H. J. Gao, B. H. Ji, Cracking and adhesion at small scales: atomistic and continuum studies of flaw tolerant nanostructures, *Modelling and Simulation in Materials Science and Engineering* **2006**, *14*, 799-816.

[116] M. Menon, D. Srivastava, I. Ponomareva, L. A. Chernozatonskii, Nanomechanics of silicon nanowires, *Physical Review B* **2004**, *70*.

[117] M. A. Makeev, D. Srivastava, M. Menon, Silicon carbide nanowires under external loads: An atomistic simulation study, *Physical Review B* **2006**, *74*.

[118] H. A. Wu, Molecular dynamics simulation of loading rate and surface effects on the elastic bending behavior of metal nanorod, *Computational Materials Science* **2004**, *31*, 287-291.

[119] J. M. Gere, *Mechanics of Materials*, Brooks/Cole, Belmont, CA **2004**.

[120] L. G. Zhou, H. C. Huang, Are surfaces elastically softer or stiffer?, *Applied Physics Letters* **2004**, *84*, 1940-1942.

[121] M. A. Meyers, K. K. Chawla, *Mechanical Metallurgy: Principles and Applications*, Prentice-Hall, Englewood Cliffs, New Jersey **1984**.

[122] F. Ma, K. W. Xu, Surface induced electron redistribution: A mechanism for mechanical strengthening of Au nanowires, *Scripta Materialia* **2006**, *55*, 951-954.